

Contents lists available at ScienceDirect

Geoderma

journal homepage: www.elsevier.com/locate/geoderma





Spatial statistical modeling of arsenic accumulation in microsites of diverse soils

Aakriti Sharma ^{a,*,1}, Joseph Guinness ^{b,2}, Amanda Muyskens ^{b,3}, Matthew L. Polizzotto ^{a,4}, Montserrat Fuentes ^{b,5}, Dean Hesterberg ^{a,6}

- ^a Department of Crop and Soil Sciences, North Carolina State University, Raleigh, NC 27695, USA
- ^b Department of Statistics, North Carolina State University, Raleigh, NC 27695, USA

ARTICLE INFO

Handling Editor: Matthew Tighe

Keywords:
Trace elements
Reactive microsites
Correlation
Pedogenic environments
Spatial heterogeneity
Soil complexity

ABSTRACT

Determining reaction mechanisms that control the mobility of nutrients and toxic elements in soil matrices is confounded by complex assemblages of minerals, non-crystalline solids, organic matter, and biota. Our objective was to infer the chemical elements and solids that contribute to As binding in matrices of soil samples from different pedogenic environments at the micrometer spatial scale. Arsenic was reacted with and imaged in thin weathering coatings on eight quartz sand grains separated from soils of different drainage classes to vary contents of Fe and Al (hydr)oxides, organic carbon (OC), and other elements. The grains were analyzed using X-ray fluorescence microprobe (µ-XRF) imaging and microscale X-ray absorption near edge structure (µ-XANES) spectroscopy before and after treatment with 0.1 mM As(V) solution. Partial correlation analyses and regression models developed from multi-element μ -XRF signals collected across $100 \times 100 \ \mu m^2$ areas of sand-grain coatings inferred augmenting effects of Fe, Zn, Ti, Mn, or Cu on As retention. Significant partial correlations (r' > 0.11) between Fe and Al from time-of-flight secondary ion mass spectrometry (TOF-SIMS) analysis of most samples suggested that Fe and Al (hydr)oxides were partially co-localized at the microscale. Linear combination fitting (LCF) results for As K-edge μ -XANES spectra collected across grain coatings typically included >80% of As(V) adsorbed on goethite, along with varying proportions of standards of As(V) adsorbed on boehmite, As(V) or As (III) bound to Fe(III)-treated peat, and dimethylarsinic acid. Complementary fits for Fe K-edge μ-XANES spectra included ≥50% of the Fe(III)-treated peat standard for all samples, along with goethite. Our collective results inferred a dominance of Fe and possibly Al (hydr)oxides in controlling As immobilization, with variable contributions from Zn, Ti, Cu, or Mn, both across the coating of a single sand grain and between grains from soils developed under different pedogenic environments. Overall, these results highlight the extreme heterogeneity of soils on the microscale and have implications on soil management for mitigating the adverse environmental impacts of As.

Abbreviations: XRF, X-ray fluorescence; XANES, X-ray absorption near edge structure; TOF-SIMS, Time-of-flight secondary ion mass spectrometry; LCF, Linear combination fitting; XAS, X-ray absorption spectroscopy; SRX, Submicron Resolution X-ray; NSLS-II, National Synchrotron Light Source-II; OC, Organic carbon; CBD, citrate-bicarbonate-dithionite; ICP-OES, Inductively coupled plasma – optical emission spectrometry.

E-mail addresses: asharm27@ncsu.edu (A. Sharma), guinness@cornell.edu (J. Guinness), muyskens1@llnl.gov (A. Muyskens), mpolizzo@uoregon.edu (M.L. Polizzotto), mfuentes@stedwards.edu (M. Fuentes), dean.hesterberg@lnls.br (D. Hesterberg).

^{*} Corresponding author

¹ Present address: Department of Plant and Soil Science, Texas Tech University, Lubbock, TX, 79409, USA.

² Present address: Department of Biological Statistics and Computational Biology, Cornell University, Ithaca, NY 14853, USA.

³ Present address: Lawrence Livermore National Laboratory, Livermore, CA 94550, USA.

⁴ Present address: Department of Earth Sciences, University of Oregon, Eugene, OR 97403, USA.

⁵ Present address: President, St. Edward's University, Austin, TX 78704, USA.

⁶ Present address: Brazilian Synchrotron Light Laboratory, Campinas, Brazil.

1. Introduction

Elevated concentrations of As have been observed in soils and groundwaters worldwide, and their negative health impacts are well recognized (Bhowmick et al., 2018; Brammer and Ravenscroft, 2009; Li et al., 2018; Ravenscroft et al., 2009; Rehman et al., 2018; Shakoor et al., 2017; Tchounwou et al., 2019). Accumulation of As in these geochemical systems can occur, for example, when naturally enriched As-bearing rocks and sediments undergo coupled biogeochemical and hydrologic processes that increase As mobility (Gillispie et al., 2016; Gillispie et al., 2019; Kocar and Fendorf, 2012; Polizzotto et al., 2008; Smedley and Kinniburgh, 2002; Wuana and Okieimen, 2011). Efforts to mitigate adverse impacts of As on human and ecosystem health have benefitted from a mechanistic understanding of the underlying biogeochemical and hydrological processes that affect As mobility.

Direct measurement of reaction mechanisms of As and other trace elements in soils is confounded by the complexity of these multicomponent systems at all spatial scales. Soils in particular have spatially varying physical, chemical, mineralogical, and (micro)biological properties as a result of long- and short-term pedogenic weathering processes (Buol et al., 2003; Hesterberg et al., 2011; Tisdall and Oades, 1982). Intimately associated minerals, non-crystalline solids, organic matter, and biomass are involved in adsorption, (co-)precipitation, redox transformations, and biological accumulation of As (Amstaetter et al., 2010; Chen and Sparks, 2015; Chen and Sparks, 2018; Fan et al., 2014; Inskeep et al., 2001; Mikutta and Kretzschmar, 2011; Otero-Fariña et al., 2017; Park et al., 2016). Consequently, soil As is distributed between multiple solid-phase chemical species at any point in time (Borch et al., 2010; Fendorf and Kocar, 2009; Fendorf et al., 2010; Gamble et al., 2018; LeMonte et al., 2017), and it is difficult to directly identify individual chemical species with a high degree of specificity (Kizewski et al., 2011). It is also challenging to measure how individual species respond to short- and long-term temporal changes in soil biogeochemical properties driven by, for example, wetting and drying or (micro)biological activity. Highly specific (e.g., molecular-level) knowledge about As adsorption/desorption, precipitation/dissolution, and redox transformations in geochemical systems is largely based on research using single or multi-component (e.g., clay-organic) model systems containing well-characterized solids. These reaction mechanisms are generally assumed to be transferable to the more complex biogeochemical matrices. However, it remains challenging to directly delineate As immobilization and release mechanisms as affected by either individual soil-matrix components or multiple, co-localized components that potentially interact.

Arsenic geochemistry is affected by the presence of multiple soil components such as (hydr)oxides of Fe, Al, and Mn, and sulfide minerals in environmentally relevant conditions such as acid sulfate soils and acid mine drainage. For example, acid sulfate soils are Fe- and S-rich and usually contain secondary Fe(III) minerals such as goethite, ferrihydrite, jarosite, and schwertmannite (Burton et al., 2021; Cheng et al., 2009; Johnston et al., 2010; Karimian et al., 2017; Paikaray, 2015; Sullivan and Bush, 2004). While these minerals are important sorbents for As, they also have potential to release As during redox transitions. For example, under reducing condition, As bound to these minerals could be released through reductive dissolution of Fe(III) oxides (Bennett and Dudas, 2003; Erbs et al., 2010; Schaefer et al., 2017). Moreover, Mn oxides present in these systems contribute as a strong oxidant, oxidizing As(III) to As(V) or Fe(II) to Fe(III) and act as a redox buffer (Borch et al., 2010; Wu et al., 2018; Ying et al., 2012). Similarly, acid mine drainage also tends to be enriched with Al, Fe, and S and traces of other contaminants. Aluminum enriched ferric oxide-hydroxide recovered from authentic acid mine drainage has high adsorption capacity of arsenate (Muedi et al., 2021). Therefore, determining the contribution of individual soil components in As immobilization in complex geochemical systems provides insights into effective management strategies for mitigating environmental impacts of As.

Soil matrix components that are responsible for As binding are often inferred from μ-XRF imaging coupled with μ-XANES spectroscopic analyses of As and different matrix elements within microsites (Burton et al., 2014; Fan et al., 2014; Gräfe et al., 2008; Landrot et al., 2012; Langner et al., 2013; LeMonte et al., 2017; Polizzotto et al., 2008; Sharma and Hesterberg, 2020; Sharma et al., 2019; Ying et al., 2013). In fact, coupling μ-XRF imaging with scanning microscale X-ray absorption spectroscopy (µ-XAS) and diffraction (µ-XRD) has yielded highly specific molecular bonding information for trace elements concentrated within homogeneous subregions of heterogeneous geochemical matrices (Manceau et al., 2014; Manceau et al., 2002). Spatial associations between soil elements are usually inferred from μ -XRF chemical images using simple (Pearson) correlations. Sharma et al. (2019) showed that this approach can be misleading because simple correlations do not decouple effects of multiple elements co-localized within the microscale soil volumes, nor do they account for autocorrelations of individual elements across a soil matrix. Moreover, one should be cautious in interpreting spatial correlation as it does not definitively show the evidence of bonding but rather only suggests its possibility. Furthermore, the spatial resolution of the microprobe could also limit the ability to decouple the effects of co-localized elements on trace metal accumulation. Many studies understandably utilized mechanisms of As binding in model systems such as high-affinity adsorption on Fe (hydr)oxides to infer binding mechanisms to similar minerals or poorly crystalline solids in soils. However, any confounding effects of less abundant matrix elements such as Mn, Ti, Cu, Zn, or Ca that might be associated with Fe (hydr)oxides are often not separated (Galkaduwa et al., 2018; Gillispie et al., 2019; Gräfe et al., 2008; Landrot et al., 2012; Schwer and McNear, 2011; Strawn et al., 2002). Analytically separating any complex interactions between abundant and minor matrix components that have been inferred to affect As immobilization (Gillispie et al., 2016; Power et al., 2005; Rao et al., 2015; Yang et al., 2010; Ying et al., 2012; Zhang et al., 2013; Zhang et al., 2018a) would provide deeper knowledge of As binding mechanisms in soils relative to model systems.

We proposed spatial-statistical approaches for separating the colocalized element effects in $\mu\textsc{-XRF}$ images of soil matrices and used these approaches to infer multiple solid phases contributing to As retention in sand-grain coatings treated with aqueous As(V) solutions (Guinness et al., 2014; Sharma et al., 2019; Terres et al., 2018). Results from a single sand grain inferred a dominance of As associated with Fe (III) and possibly Al(III) (hydr)oxides, with minor augmenting effects of co-localized Ca and Ti (Sharma et al., 2019). Here we apply these approaches to assess As retention in grain coatings from soils developed under different pedogenic environments to assess microscale matrix effects within and between soils.

Our overarching research goal is to ultimately resolve reaction mechanisms affecting trace-element binding and mobilization in soils and other complex, multi-component geochemical matrices. The specific objective of this study was to determine the consistency of short-term As accumulation in microsites from diverse soil matrices in relation to microsite elemental composition, and by inference, soil solids. Spatial and non-spatial statistical modeling was used to infer co-localized element effects on As binding within soils developed under different pedogenic environments. We hypothesized that spatial patterns of As accumulation in relation to those of matrix elements will uniquely depend on the pedogenic environment. For example, poorly drained soils that undergo more frequent oxidation and reduction are expected to contain a greater proportion of Fe in poorly crystalline forms like ferrihydrite, whereas well-drained, well-aerated soils are typically dominated by goethite (α-FeOOH) and hematite (α-Fe₂O₃) (Schwertmann, 1993). Such differences in Fe (hydr)oxide mineralogy should be important for As reactivity because poorly crystalline Fe (hydr)oxides can adsorb four- to five-fold more arsenate than goethite at a given pH (e.g., (Violante and Pigna, 2002). To test our hypothesis, we performed partial correlation and spatial and non-spatial statistical modeling of μ-XRF imaging data to assess spatial patterns of accumulated As in

relation to those of matrix elements in thin coatings of As(V)-treated sand grains (Sharma et al., 2019) isolated from different soils. Complementary As and Fe K-edge μ -XANES spectroscopy and TOF-SIMS were used for speciation modeling of both As and Fe, and to assess possible contributions of Al (hydr)oxides on As accumulation. Findings from this study provide insights to properties that control As retention in reactive geochemical microsites, which is useful for translating extensive knowledge of As reaction mechanisms from model systems to more complex, natural geochemical matrices.

2. Materials and methods

2.1. Soil sampling and sand grain collection

Samples of four soils (~2 kg each) with no known As contamination were collected from two locations in the Coastal Plain physiographic region of North Carolina. Three of the samples were collected in Nags Head Woods, two from the A (12–15 cm) and B (30–45 cm) horizons of a well-drained soil mapped as Fripp (Thermic, uncoated Typic Quartzipsamments), and one from the Bw horizon (17-21 cm) of a poorly drained Osier soil (Siliceous, thermic Typic Psammaquents) developed in the depression of a dune area that contained stagnant water. These samples are herein referred to as "Fripp A", "Fripp B", and "Osier Bw", respectively. The fourth sample was collected within the Greenville, NC city limits, where the B horizon (30-40 cm) of a well-drained Buncombe soil (Mixed, thermic Typic Udipsamments) on a natural levee was sampled, i.e., "Buncombe B". The samples were placed into Ziploc® plastic bags, transported on ice, and stored in a refrigerator without drying until physically fractionated to collect sand grains. No special precautions were taken to exclude oxygen during sampling and storage. Measurements on whole soil samples included soil pH in 1:1 w/v soil: water (Thomas, 1996), texture by the hydrometer method (Gee and Bauder, 1986), and total C using a CHN Elemental Analyzer (PerkinElmer model 2400), which was assumed to represent total organic carbon (OC) on these acidic soil samples. Oxalate and citratebicarbonate-dithionite (CBD) extractable Fe and Al were measured on separate soil samples following Jackson et al. (1986). Pseudo-total elemental contents were measured by ICP-OES following acid digestion using concentrated HNO3 and HCl, and H2O2 (30%) according to EPA Method 3050B (EPA, 1996).

Quartz sand grains were fractionated from each soil sample by dispersion in deionized $\rm H_2O$ and wet sieving as described in Sharma et al. (2019). Two sand grains from each of the four soil samples were selected under an optical microscope for $\mu\text{-XRF}$ imaging and spectroscopic analyses and are herein labeled, for example, "Buncombe B #1" and "Buncombe B #2". The selected grains had visibly thin weathering coatings of reddish-colored Fe (hydr)oxide (pictures in Appendix Fig. A.1), and a relatively flat area rather than crevices was chosen for analyses to avoid signal attenuation.

2.2. Micro- X-ray fluorescence imaging

Spatial patterns of As accumulation in relation to detected soil matrix elements in each sand-grain coating were assessed using μ -XRF imaging on the Submicron Resolution X-ray Spectroscopy (SRX) beamline (5-ID) at the National Synchrotron Light Source-II (NSLS-II), Brookhaven National Laboratory (Chen-Wiegart et al., 2016), as described in Sharma et al. (2019). Here, soil matrix elements are referred to the elements that are inherently present in the sand-grain coating. The beamline optics and detector set up were similar to that described in Sharma et al. (2019), except that a constant beam current of 300 mA was used and the sample stage was perpendicular to the beam to maximize spatial resolution. All μ -XRF images were collected at 13.5 keV with 0.5 s dwell time and 1 μ m \times 1 μ m pixel size. We merged fluorescence signals collected by each of three elements of a Vortex detector that was offset by 15° from the sample plane. Element-specific fluorescence intensities at each pixel

were extracted by full spectral fits (Fig. A.6) using the PyXRF software (Li et al., 2017) as described in Sharma et al. (2019). These $100 \times 100 \ \mu m^2 \ \mu$ -XRF images are herein identified as "ROI-100a", whereas separate images ("ROI-100b") were collected with a different sample/detector geometry to identify locations for collecting μ -XANES spectra as described below.

A unique aspect of our research approach is that we assessed shortterm reactivity of the sand grain coatings with As(V) directly by acquiring µ-XRF images before and after treatment with an aqueous arsenate solution, as described by Sharma et al. (2019). Basically, an initial fly scan image was collected across one or, in some cases two, 100 \times 100 μm^2 areas of a sand grain before As(V) treatment to determine the multi-element composition of the weathering coating. The quartz core is considered to be unreactive, and the quartz attenuates the X-ray beam so that multi-element fluorescence signals mainly arise from the front surface coating, which is effectively a "natural thin section" (Sharma et al., 2019). After imaging, the kinematic holder with the mounted grain was removed from the beamline and reacted in the laboratory for 30 min with 0.1 mM Na₂HAsO₄·7H₂O in a 0.1 mM NaCl background solution. Excess aqueous As and perhaps weakly bound As were removed by rinsing the treated grain four times with 150 µL aliquots of deionized H₂O. The treated grain was dried under N₂(g), re-mounted on the beamline and aligned, and a second µ-XRF image was collected across the same, As(V)-treated ROI-100a [see details in Sharma et al. (2019)]. The As(V) treatment solution was pre-adjusted to pH 5.5, consistent with the average pH of 5.5 \pm 0.3 measured on our bulk-soil samples. The 30-minute reaction time was chosen mainly to focus on adsorption mechanisms at the initial part of the reaction. Hence, microscale spatial patterns of As accumulated in the grain coatings should reflect soil components that immobilize As during an initial exposure of soil to arsenate contamination, including fast adsorption reactions (Sparks, 1999). For example, Raven et al. (1998) showed that adsorption of aqueous arsenate by reactive soil components such as ferrihydrite can reach steady state within ≤5 min when treated at sub-maximal adsorption levels of ~ 300 mmol As/kg.

For the second grain from the Buncombe B soil (Buncombe B #2) we performed a more intensive set of measurements to assess variability in μ-XRF images of accumulated As due to any potential beam-induced changes, and between two locations on the same sand grain. These analyses indicated whether any variations in As accumulation in relation to soil matrix elements across sand grains from different soils could be uniquely ascribed to pedogenic effects, beyond variability on a single or multiple grains from the same soil sample. Two $100 \times 100 \,\mu\text{m}^2$ ROIs (R1 and R2) separated by <1 mm on the Buncombe B #2 grain were each imaged once before and twice after applying the As(V) treatment. These images are herein designated as "Buncombe B #2-R1-1" and "Buncombe B #2-R1-2" (grain 2, ROI1, replication 1 and 2), and "Buncombe B #2-R2-1" and "Buncombe B #2-R2-2". Overall, duplicate μ-XRF images were collected from two different areas of one Buncombe B soil sand grain, and single μ-XRF images were collected on the remaining sand grains collected from four different soil samples.

2.3. Micro-XANES spectroscopy

To select points for $\mu\text{-XANES}$ analyses, separate $\mu\text{-XRF}$ images of 100 \times 100 μm^2 were collected on one sand grain from each of the four soil samples (referred to as ROI-100b) with the Vortex detector set at 45° to diminish background scattering contributions to spectra. The ROI-100a and ROI-100b regions were visually judged, based on physical features of the sand grains, to be essentially overlapped for the Buncombe B and Fripp B soil samples. However, for the Fripp A and Osier Bw samples the two ROIs did not overlap and were offset to a region of greater As fluorescence signal to obtain higher quality $\mu\text{-XANES}$ spectra. Point $\mu\text{-XANES}$ spectra were collected at both the As and Fe K-edges as single scans across multiple spots of varying fluorescence signals. Each $\mu\text{-XANES}$ spectrum was collected between 11,842 and 11942 eV for As

or between 7087 and 7187 eV for Fe using a minimum step size of 0.25 eV across the edge region and 0.1 or 0.5 s dwell time, depending on signal intensity. The energy of the As μ -XANES spectra was calibrated to the white line maximum set at 11874 eV for As(V) in a natural scorodite inclusion (Sharma et al., 2019), and that of Fe µ-XANES spectra was calibrated to the first derivative maximum (set at 7112 eV) of a spectrum collected in fluorescence mode from a 5 µm thick Fe foil. Linear combination fitting analysis for As μ-XANES included spectra from various Fe-, Al-, and Ca-bonded arsenate or arsenite standards in adsorbed or mineral forms that were collected previously at unfocused beamlines (Lopez et al., 2018), along with As₂O₅ and As₂O₃ salts (Table A.1, Fig. A.2). Standards for fitting Fe μ -XANES spectra included ferrihydrite, hematite, magnetite, ferric glass [Fe(III) co-precipitated in aluminosilicate glass], goethite, pyrite, siderite, and a Fe(III)-treated peat sample (Fig A.2). The Fe(III)-treated peat standard was prepared by reacting 3600 mmol Fe(III) (as FeCl₃) per kg Pahokee peat in a 50 mM KCl solution at pH 6 for 42 h. EXAFS spectra of this standard (not shown) showed a higher-shell peak that was similar but not as intense as that of ferrihydrite, indicating a combination of Fe-hydroxide polymers as well as Fe(III)-NOM complexes. Other standards included here are described elsewhere (Rivera et al., 2015).

The u-XANES spectra were analyzed using IFEFFIT under the Athena interface (Ravel and Newville, 2005). We merged µ-XANES spectra from soil microsites of similar chemical composition to obtain higher quality spectra for selecting appropriate fitting standards. Given a strong As-Fe partial correlation (discussed below), for each grain we first grouped and merged non-normalized As μ -XANES spectra into "high" and "low" Fe groups, and separately Fe μ-XANES spectra into "high" and "low" As groups. The merged spectra within each group had lower spectral noise than spectra from individual spots and were used in initial fitting analysis to select a subset of standards to include in fits to spectra from individual spots (Sharma et al., 2019). The high vs. low groupings were determined as having >50% or $\le 50\%$ of the maximum fluorescence signal for the complementary element for all spots on a given sand grain, and more than half of the spots with high or low As corresponded with those with high or low Fe, respectively. The spectra for As and Fe standards collected at bulk-sample beamlines were baseline subtracted using a linear function between -200 and -30 eV and normalized using a linear function between 45 and 900 eV, all relative to E0 taken as the first derivative maximum. The µ-XANES spectra from sand grains were baseline subtracted between -35 and -10 eV. However, sample μ-XANES spectra were collected over a shorter relative energy range (approximately -25 to 75 eV) and did not exhibit an extended flat postedge region like those of bulk standards. Therefore, the normalization range for μ-XANES spectra was selected, along with the "flatten" function in Athena (Kelly et al., 2008), so that the post-edge region of μ-XANES spectra overlaid with spectra of bulk standards exhibiting similar post-white line features.

The initially grouped As and Fe μ-XANES spectra were fit with all standards over an energy range of −10 to 25 eV relative to E₀ for As-XANES or −17 to 35 eV for Fe-XANES. Fits were done using a modification of the standard-elimination approach described by Manceau et al. (2012), and allowing an energy shift of up to \pm 0.25 eV for individual standards. The details of the μ -XANES fitting method used here can be found in Sharma et al. (2019). Weighting factors on fitting standards were not constrained, but were renormalized to sum to 100% (Kelly et al., 2008). The LCF results of merged Fe-XANES from different soil environments showed that these spectra could all be fit with combinations of goethite and peat reacted with Fe(III) at a loading of 3600 mmol kg⁻¹ [Fe(III)-peat 3600] standard. These two standards, which represent crystalline and poorly crystalline phases, were then used to fit Fe μ-XANES spectrum from individual spots of all samples. For As, however, individual spectra from low As/Fe regions were too noisy (Fig. A.5) to obtain reliable fits. Consequently, merged As μ-XANES spectra with low and high As/Fe regions collected from a given sand grain were fit, and LCF results included different combinations of these standards: As

(V) bound to goethite, As(V) bound to Fe(III)-treated peat, As(V) adsorbed on boehmite, dimethylarsenic acid, and As(III) bound to Fe (III)-treated peat.

2.4. TOF-SIMS analysis

We used TOF-SIMS at the NC State Analytical Instrumentation Facility (NCSU-AIF, 2018), with a pixel size of 0.39 $\mu m \times 0.39~\mu m$ and estimated penetration depth of 3 nm. Spatial distributions of Al and C in relation to Fe was determined in areas within 100 μm of ROI-100b of As (V)-treated sand grains. We followed the experimental procedure described by Sharma et al. (2019), except that initial sputtering was done for 68 s to remove surface contamination before collecting data. Arsenic was not detected by TOF-SIMS.

2.5. Statistical analyses

The μ -XRF data normalized to the incoming X-ray intensity (I_0) were natural log (ln) transformed, and partial correlation, and spatial-likelihood linear regression (spatially correlated error model—also referred to as spatial models) and simple multiple linear regression (independent error model—referred to as non-spatial models) were conducted using R statistical software (RStudio—Version 1.1.383) as described by Sharma et al. (2019). The log transformation was applied to the data to approximate a normal distribution, which is a criterion for conducting linear correlation and regression models. Because some features of soil matrix elements in images were visibly changed before and after the As(V) treatment (Sharma, 2019), statistical relationships were analyzed between fluorescence signals for As and matrix elements after the treatment to improve spatial registry of all elements.

Statistical modeling to describe spatial patterns of As accumulation on As(V) treated sand grains in relation to native soil matrix elements imaged by µ-XRF involved a combination of spatial and non-spatial regression modeling (Sharma et al., 2019). Spatial likelihood linear models fit using a 'GpGp' package in R (Guinness, 2018a) were used to select matrix elements that are significant predictors of As while accounting for autocorrelation (Beale et al., 2010), which is inherent in geochemical matrices showing element hotspots. Residuals were assumed to follow a Gaussian process and a Matérn isotropic covariance function (Guinness, 2018b; Minasny and McBratney, 2005; Minasny and McBratney, 2007) with parameters of variance, range, smoothness, and nugget. To simplify models for predicting As accumulation to three or less matrix elements, significant predictors in spatial models having regression coefficients $< \pm 0.05$ were excluded, and the remaining predictors were used to develop non-spatial linear-regression models, which give better predictions of accumulated As than spatial models (Sharma et al., 2019).

Furthermore, to assess whether the variation in As(V) retention within soils was as significant as the variation between soils, we performed the log likelihood ratio test. The log likelihood ratio test informed whether different models are needed to describe variability of accumulated As within soils. We combined the data collected across ROI-100a on each of the two replicated grains from each soil and fit a single non-spatial model to the combined dataset. Then we used the log likelihood ratio test to determine whether non-spatial models fit to individual datasets were significantly ($\alpha=0.05$) different than those fit to the combined datasets. Similarly, we also tested datasets from two regions within the same grain.

3. Results

3.1. Soil properties

The soil samples from which sand grains were isolated were mostly of fine sand texture, with pH between 5.3 and 5.9 (mean $=5.5\pm0.3;$ Table 1). The samples varied in contents of oxalate or CBD-extractable

Table 1Selected chemical and physical properties of bulk soil samples from which sand grains were isolated. ^a

Soil sample	Drainage class	pН	Texture	Fe _{ox}	Fe_{CBD}	Fe _{ox}	Al _{ox}	Al_{CBD}	OC
				mg/kg	mg/kg	Fe _{CBD}	mg/kg	mg/kg	% (w/w)
Buncombe B	Well-drained	5.4	SL	1415 ± 141	2264 ± 2	0.63	303 ± 42	549 ± 25	0.17 ± 0.02
Fripp A	Well-drained	5.4	FS	478 ± 9	1329 ± 17	0.36	159 ± 5	348 ± 13	0.55 ± 0.03
Fripp B	Well-drained	5.3	FS	879 ± 6	2099 ± 11	0.42	255 ± 0	500 ± 6	0.24 ± 0.01
Osier Bw	Poorly-drained	5.9	FS	<6	151 ± 13	< 0.04	<6	115 ± 11	0.27 ± 0.04

^a ox = oxalate extractable; CBD = citrate-bicarbonate-dithionite extractable; OC = organic carbon; FS = fine sand; SL = sandy loam; Numbers represent mean \pm standard deviations of duplicate measurements. Suffix on the sample name indicates horizon designation.

Fe and Al, and contents of organic C and other matrix elements (Tables 1, A.2). These differences reflect different pedogenic weathering environments. The sample from the poorly drained Osier soil contained one to two orders of magnitude less oxalate- and CBD-extractable Fe and Al than those from the well-drained Buncombe and Fripp soils. Oxalate and CBD-extractable Fe are indicative respectively of poorly crystalline + organic-matter associated Fe and total free Fe (hydr)oxides including crystalline forms (Jackson et al., 1986). The ratio of oxalate/CBD Fe is generally expected to be greater in poorly drained soils (Schwertmann, 1993), but this trend did not hold for the Osier Bw sample, perhaps because of its overall lower extractable Fe contents (Table 1). Ratios of oxalate/CBD Fe between 0.4 and 0.6 for the other three samples suggest that Fe is nearly equally distributed between poorly crystalline or organic-matter bound Fe and crystalline Fe (hydr)oxide minerals in the bulk soil samples. Similarly, oxalate- and CBD-extractable Al contents of the soil samples suggest the presence of both poorly crystalline Al hydroxides and Al co-precipitated with Fe (hydr)oxides (Jackson et al., 1986). Although the characterization data in Table 1 indicate that the soil samples vary in arsenate sorption properties related to forms and amounts of Fe and Al (hydr)oxides and organic matter, these bulk-soil characteristics are not necessarily representative of those for surface coatings of our selected sand grains, nor within the specific microsites analyzed by synchrotron μ -XRF and μ -XANES.

3.2. Spatial patterns of accumulated As and soil matrix elements

Fig. 1 shows μ-XRF images of As before and after As(V) treatment along with images of Fe, Mn, and Ti after As(V) treatment, acquired across ROI-100a for one of the two sand grains collected from each soil sample. The remaining μ -XRF images are included in Appendix Fig. A.3. Average natural log-transformed values of fluorescence signals across each image for each element are shown in Table A.3. We consider the $\mu\text{-}XRF$ signals across a given ROI to generally reflect relative elemental contents of microsites within these regions, and averaged fluorescence signals were considered to gauge relative abundances of elements between the $100 \times 100 \ \mu m^2$ regions imaged. However, note that the coating thickness of the sand grain was not measured in this study, and the variability in thickness affects the fluorescence intensities. Nevertheless, our results should be minimally affected as our objective was to determine the contribution of matrix elements to accumulate As in a given microsite, and the effect of coating thicknesses were assumed to be thin enough that any variations in thickness would all similarly affect elemental fluorescence signals within a microsite. Prior to the As(V) treatment, ROI-100a showed detectable As signals from all samples (Figs. 1 and A.3). However, after As(V) treatment the average As fluorescence signal for Buncombe B #1 and Fripp B #1 increased by ~ 14 fold and that for the remaining samples increased by up to 6.4 fold,

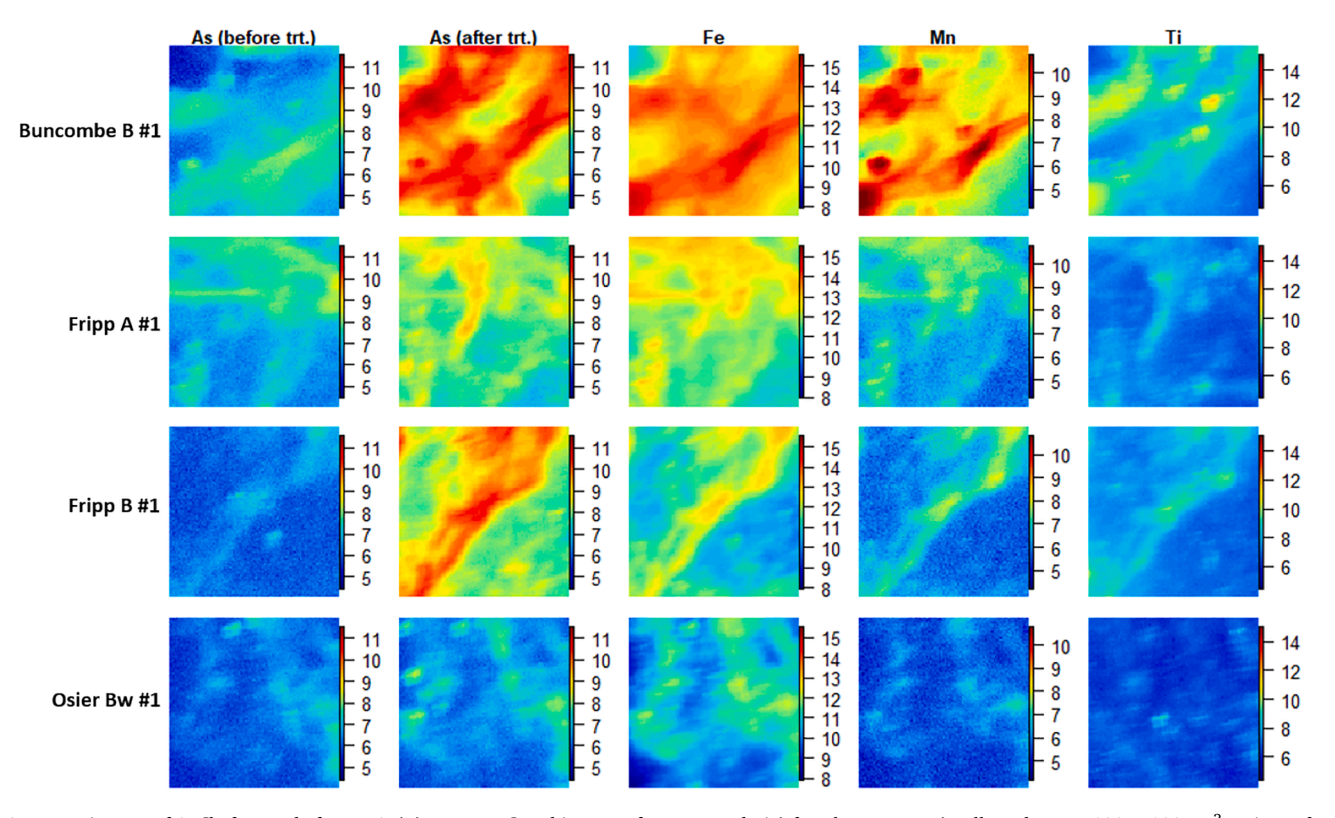


Fig. 1. μ -XRF images of As [before and after an As(V) treatment] and images of Fe, Mn, and Ti (after the treatment) collected across $100 \times 100 \ \mu m^2$ regions of sand grains (ROI-100a). Brighter colors in the μ -XRF images represent greater natural log-transformed fluorescence signals for each element analyzed.

except for Osier Bw #2. The latter sample showed only 22% increase in As signal, suggesting that As(V) accumulated to a lesser extent in this grain (Figs. 1 and A.3; Table A.3). Spatial distribution of matrix Fe, Mn, Ti, and Zn shown by $\mu\text{-XRF}$ images as well as scatter plots of As vs. Fe, Mn, Zn and Ti (Fig. A.4) indicated that these elements are at least partially co-localized in all samples. However, spatial distribution of Si did not follow spatial pattern of any native matrix elements, which indicates that Si signals are likely contributed from both the quartz core of the sand grain as well as any Si associated with the minerals in the grain coating. Overall, visible spatial patterns of accumulated As(V) were most similar to those of Fe and Mn, and to a lesser extent Ti, Zn, and Cu.

Fig. 2 shows μ -XRF images of As and Fe acquired from ROI-100b of As(V) treated sand grains where As and Fe μ -XANES were collected, and Fig. 3 shows corresponding Fe⁺, Al⁺, and C⁻ collected by TOF-SIMS within 100 μ m of ROI-100b. For all four μ -XRF images, visible spatial patterns of accumulated As(V) followed those of Fe (Fig. 2). TOF-SIMS images showed visibly similar spatial patterns of Fe and Al especially for Buncombe B #1 and Fripp B #1, and to a lesser extent for Fripp A #1 and Osier Bw #2. No visible similarities in spatial patterns of C and Fe or Al was found, perhaps because the C signals were considerably weaker than those of the metals (Fig. 3). TOF-SIMS measured Al signals were at least two times greater than those of Fe. Furthermore, TOF-SIMS measured Al content in the top 3 nm probed by this analysis appeared to be greater in Buncombe B #1 followed by Fripp B #1, which is also supported by the results from bulk-soil analysis of Al content (Table A.2).

3.3. Correlations of As and soil matrix elements

Partial correlation coefficients (r') between (log-transformed) $\mu\text{-XRF}$ signals of As and native soil matrix elements across $100\times100~\mu\text{m}^2$ ROIs of sand grains (Table 2) inferred that the degree of heterogeneity of matrix elements affects As accumulation irrespective of pedogenic environment. Our results showed differences in significant partial correlations from two regions of the same sand grain separated by <1 mm, as well as between the two sand grains from the Buncombe B horizon (#1, #2 - Table 2). It is noteworthy that the different ROIs on these two

grains have different overall average (ln-transformed) signals from the matrix elements, which potentially affects matrix element speciation and reactivity with As(V). Note that such differences in r' values between the two sand grains within the soil were also evident in the other three soils that we studied.

Statistically significant ($\alpha = 0.05$) values of r' from μ -XRF images ranged from -0.21 to 0.61 for ROI-100a and from 0.05 and 0.55 for ROI-100b. Note that ROI-100b at least partially overlapped with ROI-100a in some cases. Of 13 regions in ROI-100a and ROI-100b imaged, the greatest positive correlations were found between accumulated As and Fe for nine ROIs, between As and Mn for two ROIs, and between As and Ti or Zn for one ROI each; and negative correlations were found in three cases between As-Mn, As-Ti, and As-Zn. Also, note that partial correlation results of repeated μ -XRF images in region R1 and R2 of Buncombe B grain #2 showed identical r' values for As-Fe and As-Ti, however, r' for As-Cu showed a difference of 0.11 unit (Table 2), indicating negligible beam-induced changes. Collectively, our partial correlation results infer a dominance of Fe (hydr)oxides in augmenting As accumulation for all samples. However, a statistically significant ($\alpha = 0.05$) but weak positive partial correlation (r' > 0.11) between Fe and Al determined by TOF-SIMS analysis of four sand grains, suggested that Al (hydr)oxides likely contributed to As accumulation, consistent with findings of Sharma et al. (2019). In fact, the TOF-SIMS analyses indicated greater Al than Fe in the sand grain coatings measured (Fig. 3), at least in the top \sim 30 Å probed by this analysis.

3.4. Statistical models for predicting As accumulation

Spatial and non-spatial regression models (Tables 3, A.4 and A.5) that predicted As accumulated in ROI-100a and ROI-100b of sand grains also inferred that microscale heterogeneity of elements within soil microsites affect As accumulation regardless of the soil pedogenic environment. Models from sand grains within the same soil, as well as from two regions of the same sand grain involved different combinations of predictor elements in predicting As accumulation or had different regression coefficient values for the given predictor (e.g., Fe, Zn, and Ti). Of 15 spatial models developed for ROI-100a and ROI-100b, eight of

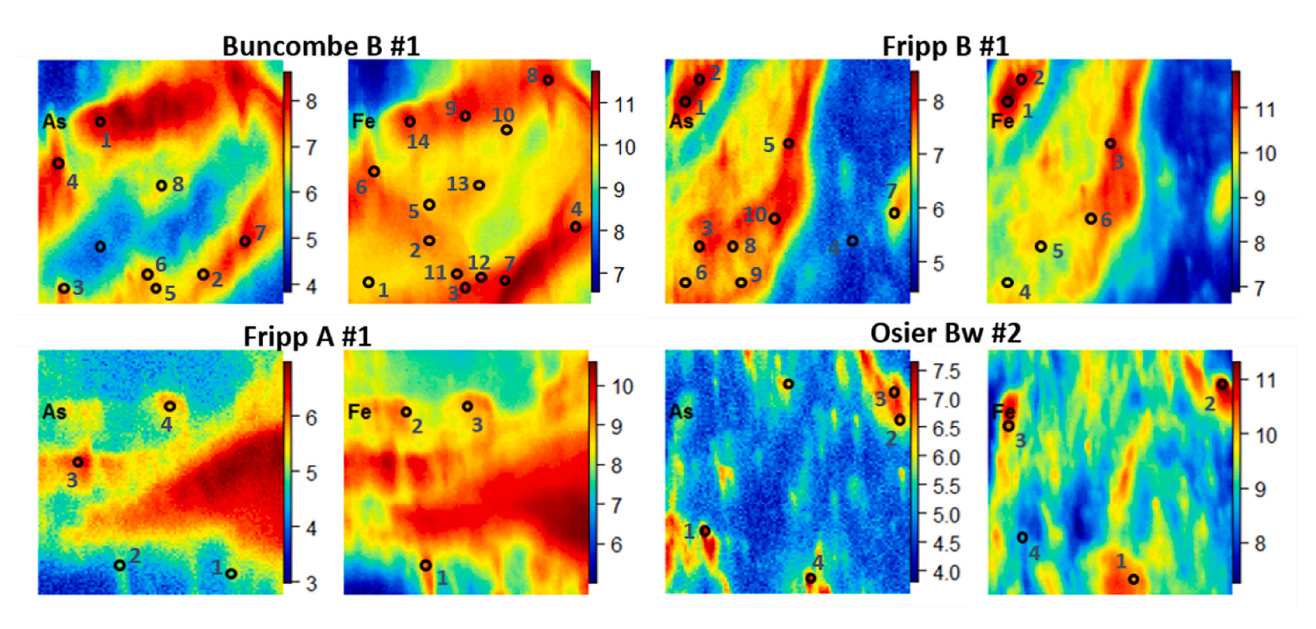


Fig. 2. μ -XRF images of As and Fe acquired across $100 \times 100 \ \mu\text{m}^2$ regions (ROI-100b) of As(V) treated sand-grains showing numbered spots (black circles) where individual As and Fe μ -XANES spectra were collected. Brighter colors in the μ -XRF images represent greater natural log-transformed fluorescence signals for each element analyzed. Spots that have >50% or \le 50% of the maximum fluorescence signal of As/Fe were designated as high (H) or low (L) As/Fe spots for μ -XANES analysis.

A. Sharma et al. Geoderma 411 (2022) 115697

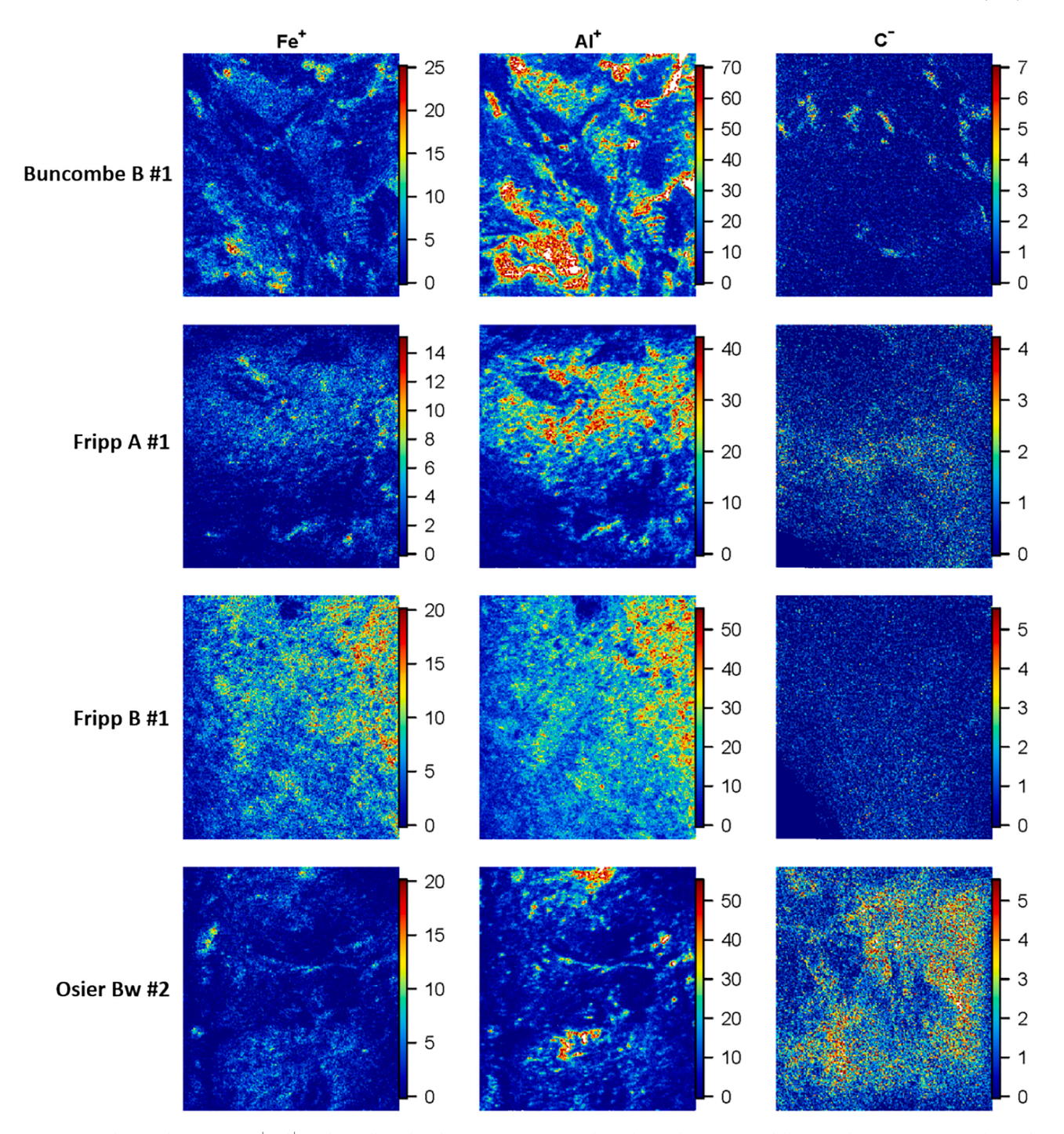


Fig. 3. TOF-SIMS elemental images of Fe^+ , Al^+ , and C collected within 100 μm of ROI-100b on the sand grains from different soil environments. Brighter colors in the elemental images indicate greater ion counts on a linear scale.

them included four or five significant ($\alpha=0.05$) predictors. In all spatial models Fe was the predictor with the greatest regression coefficient, and in 12 of the models Fe had regression coefficients ≥ 0.5 . Elimination of any predictor with coefficients $\leq \pm 0.05$ in the spatial models produced all non-spatial models with a maximum of three predictors. For essentially all cases, the non-spatial models gave better predictions (greater R²) but greater Akaike Information Criteria (AIC) values than the spatial models (Tables 3; A.4; A.5), consistent with Sharma et al. (2019). The AIC values estimate the relative quality of each statistical model for a given set of data based on the number of parameters included in the

model and the log likelihood value (Ma et al., 2017). Fig. 4 compares how well the non-spatial models predict As fluorescence signals for different samples.

Iron was among the strongest predictors for non-spatial models along with Cu, Zn, Ti, or Mn (Table 3 and A.5). Additionally, most of the models in ROI-100b and a few in ROI-100a also showed that Fe was the sole predictor of As accumulation, consistent with As $\mu\text{-XANES}$ fit results which showed a dominance of Fe-bonded As(V) standards (discussed below). It is important to note that the $\mu\text{-XRF}$ fluorescence signals for Fe were orders of magnitude greater than those for these other elements

Table 2 Partial correlation coefficients (r') showing significant ($\alpha=0.05$) correlation between natural log-transformed μ -XRF signals of As and soil matrix elements across ROI-100a and ROI-100b, and between TOF-SIMS signals of Fe and Al (ROI-100b only) for sand grain samples. ^{a.}

Sample ID	Matrix Elements	Partial correlation (r')
ROI-100a (μ-XRF)		
Buncombe B #1	Mn	0.41
	Fe	0.20
	Zn	-0.21
Buncombe B #2-R1-1	Fe	0.47
	Cu	0.40
Buncombe B #2-R1-2	Cu	0.51
	Fe	0.47
Buncombe B #2-R2-1	Ti	0.37
	Fe	0.30
Buncombe B #2-R2-2	Ti	0.37
	Fe	0.30
Fripp A #1	Fe	0.40
	Ti	0.35
Fripp A #2	Fe	0.54
	Ni	0.24
Fripp B #1	Fe	0.61
	Mn	-0.21
Fripp B #2	Fe	0.59
	Ti	0.37
Osier Bw #1	Fe	0.42
	Ni	0.27
Osier Bw #2	Fe	0.21
	Ti	-0.17
ROI-100b (μ-XRF)		
Buncombe B #1	Mn	0.51
	Fe	0.08
Fripp A #1	Zn	0.55
	Fe	0.53
Fripp B #1	Fe	0.46
• •	Ti	0.36
Osier Bw #2	Fe	0.31
	Cr	0.25
ROI-100b (TOF-SIMS)		
Buncombe B #1	Fe-Al	0.03
Fripp A #1	Fe-Al	0.26
Fripp B #1	Fe-Al	0.11
Osier Bw #2	Fe-Al	0.24

 $[^]a$ For the Buncombe B #2 sand grain, "R1" and "R2" represent two different $100\times100~\mu\text{m}^2$ regions, and "-1", and "-2" represent duplicated images of the same ROI.

(Figs. 1, A.3; Table A.3), although natural log transformation diminishes this discrepancy in the regression models. In all but one case (Zn in model 1), regression coefficients were positive and inferred an augmenting effect of the predictor elements on As accumulation (Table 3

and A.5). Note that the poor model prediction was found for Osier Bw #2 in ROI-100a (R 2 = 0.01) and ROI-100b (R 2 = 0.26), perhaps because As accumulation was minimally greater than the native As in this grain (Fig. A.3).

Our results from log likelihood ratio tests of non-spatial regression models (Table A.6) showed significant differences between the models for sand grains from the same soil, as well as for two regions of the same sand grain. Thus, unique models were generally needed to describe As accumulation from any μ -XRF image collected on any area of a sand-grain coating. These results infer that the variability of As-matrix element relationships within a given soil can be as significant as the variability between soils from different pedogenic environments. Moreover, the result of this test for repeated μ -XRF images from the same area on the same grain were not statistically significant, which indicated that beam-induced effects have minimal contribution to variability in μ -XRF images. Overall, our regression models inferred that soil components containing multiple matrix elements, e.g., Fe, Mn, and perhaps Ti (hydr)oxides contribute to As sorption within the soil microsites of our samples, with an augmenting effect of Cu or Zn in many cases.

3.5. Speciation of soil As and Fe

Variations in linear combination fitting results for As and Fe μ-XANES spectra showed the extent of spatial variations in As and Fe speciation within soil microsites on grains from within or between different pedogenic environments (Tables 4-6; Figs. 5 and 6). Overall, the As μ -XANES spectra collected on the sand grains had visibly similar spectral features, but showed minor differences in white line intensities or breadth (Fig. 5). Similarly, Fe μ-XANES spectra showed only minor visible differences in spectral features (Figs. 5 and 6). Fitting results for As included >80% of a standard of As(V) adsorbed on goethite for all but the Osier Bw #2 high-As sample, along with various proportions of three other standards (Table 4). The standard of As(V) adsorbed on Al oxyhydroxide (boehmite) accounted for most of the remaining spectral features in five of the samples, with the Osier Bw #2 high-As sample including 8% As(III) in the fit. Although the averaged Fe µ-XANES spectra for high and low-As spots were largely fit with a standard of Fe (III) bound with peat at 3600 mmol Fe kg⁻¹ peat (Table 5), fits to spectra from individual spots showed greater variation between this and a goethite standard, especially for the Buncombe B #1 sample for which the most spots were analyzed (Table 6).

The standard of As(V) adsorbed on goethite dominated the fits for As $\mu\text{-XANES}$ merged for low- and high-Fe regions, however, no statistically significant ($\alpha=0.05$) correlation was found between fitted proportions of this standard (Table 4) and corresponding ln-transformed $\mu\text{-XRF}$ signals for Fe averaged across all spots within the group. Similarly, the fitted proportions of the two Fe standards to Fe $\mu\text{-XANES}$ spectra showed

Table 3 Non-spatial models for describing As accumulation in relation to soil matrix elements based on μ -XRF fluorescence signals from elements in ROI-100a imaged on sand grains. Models include significant predictors with coefficients \geq 0.05 from corresponding spatial likelihood models shown in Table A.4, and "e" represents model residuals. The AIC values estimate the relative quality of each statistical model for a given set of data based on the number of parameters included in the model and the log likelihood value.

Sample ID	Eq. no	General form of the Models $(As = constant + predictor 1 + predictor 2 + + e)$				Log likelihood	AIC	R^2
		Constant	Predictor 1	Predictor 2	Predictor 3			
Buncombe B #1	1	7.95	0.74 Mn	0.40 Fe	–1.12 Zn	-7218.4	14446.8	0.64
Buncombe B #2-R1-1	2	-5.73	0.97 Cu	0.51 Fe		-4502.7	9013.4	0.38
Buncombe B #2-R1-2	3	-5.87	0.97 Cu	0.52 Fe		-4643.9	9295.7	0.44
Buncombe B #2-R2-1	4	-0.98	0.67 Fe	0.18 Zn		-3327.4	6662.9	0.78
Buncombe B #2-R2-2	5	-0.90	0.67 Fe	0.17 Zn		-3373.0	6753.9	0.78
Fripp A #1	6	-1.23	0.57 Fe	0.26 Ti	0.05 Zn	-504.3	1018.6	0.72
Fripp A #2	7	-11.27	0.80 Ti	0.67 Zn	0.62 Fe	-7817.1	15644.3	0.67
Fripp B #1	8	-2.77	1.01 Fe			-2301.7	4609.4	0.85
Fripp B #2	9	-4.87	0.87 Fe	0.48 Zn		-9305.4	18618.8	0.66
Osier Bw #1	10	-3.66	0.63 Zn	0.50 Fe		-716.6	1441.2	0.67
Osier Bw #2	11	5.73	0.14 Fe			-9226.7	18459.3	0.01

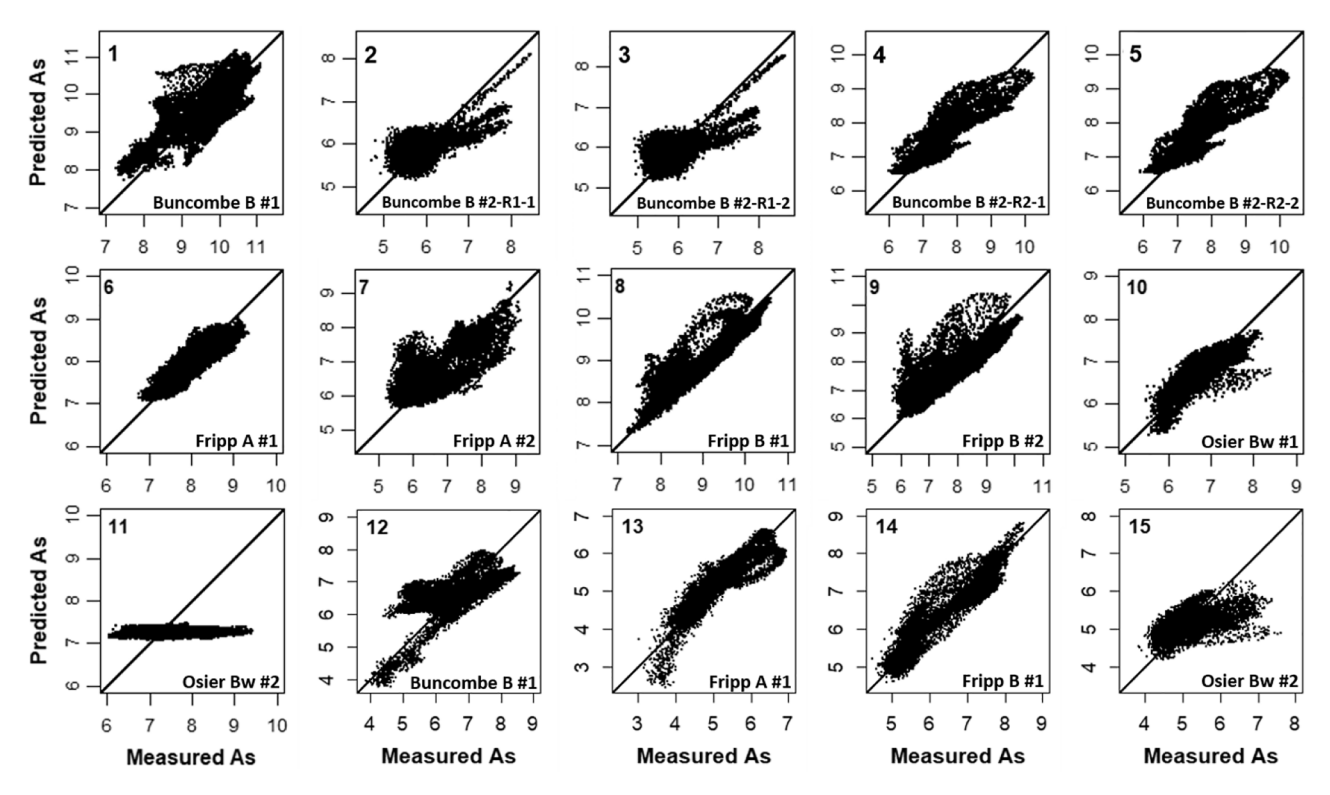


Fig. 4. Scatter plots of predicted vs measured natural log-transformed As μ-XRF signals for non-spatial predictive models developed for ROI-100a and ROI-100b. Plot labels correspond with equation numbers in Tables 3 and A.5, and 1:1 lines represent a perfect match between data and predictions.

Table 4 Linear combination fitting results showing combinations of standards giving best fits to As μ -XANES spectra collected and merged for high (H) and low (L) Fe regions on a sand grain selected from each of four soil samples (fits are overlaid on spectra in Fig. 5a).

Sample ID	Proportions of standards \pm uncertainty a						
	As(V)-goethite (adsorbed)	As(V)-Fe-peat	As(V)-Fe-peat As(V)-boehmite (adsorbed)		DMA As(III)-Fe-peat		
Buncombe B #1 - H	82 ± 2			18 ± 3		0.0073	
Buncombe B #1 - L	87 ± 5		13 ± 5			0.0015	
Fripp A #1 - H	83 ± 7		17 ± 7			0.0032	
Fripp A #1 - L	89 ± 7	11 ± 7				0.0045	
Fripp B #1 - H	87 ± 5		13 ± 5			0.0019	
Fripp B #1 - L	87 ± 5		13 ± 5			0.0021	
Osier Bw #2 - H	64 ± 10		28 ± 12		8 ± 3	0.0129	
Osier Bw #2 - L	89 ± 2			11 ± 2		0.0091	

a As(III) or As(V)-Fe-peat represents As(III) or As(V) sorbed on peat pretreated with 2400 mmol Fe/kg, and DMA = dimethylarsinic acid.

no significant ($\alpha=0.05$) correlation with the corresponding Intransformed Fe fluorescence signals from ROI-100b for all four sand grains. In general, these results suggest that the proportion of Feassociated As species does not change systematically with Fe content of microsites. Microsite characteristics other than Fe content, possibly Al content or effects of other elements could perhaps affect the proportions of Fe associated As species, and Fe speciation.

4. Discussion

4.1. Soil microsites selection

Soil samples from which the sand grains were isolated for this study had similar pH but were generally weathered under different drainage conditions, and they showed differences in extractable Fe and Al, organic C, and overall elemental composition (Tables 1, A.2). Studies have shown that soil sand fractions can adsorb as much as 60% of the total P which was found to be associated with Fe rich amorphous aluminosilicates in sand-grain coatings (Arai and Livi, 2013). Because As (V) has similar chemical structure to phosphate, a substantial amount of

Table 5 Linear combination fitting results showing combinations of standards giving best fits to Fe μ -XANES spectra collected and merged for high (H) and low (L) As regions on a sand grain selected from each of four soil samples (fits are overlaid on spectra in Fig. 5b).

Sample ID	Proportions	R-factor	
	goethite	Fe(III)-peat 3600 ^a	
Buncombe B #1 - H		100 ± 11	0.0008
Buncombe B #1 - L	45 ± 6	55 ± 5	0.0007
Fripp A #1 - L		100 ± 7	0.0010
Fripp B #1 - H	48 ± 4	52 ± 3	0.0006
Fripp B #1 - L		100 ± 6	0.0009
Osier Bw #2 - H		100 ± 7	0.0009
Osier Bw #2 - L		100 ± 7	0.0019

^a Fe(III) treated peat samples with Fe reacted at 3600 mmol Fe/kg peat.

As(V) is also expected to be adsorbed in the sand-grain coatings, and hence quartz sand grains with surface coatings were selected for analyses. The advantage of analyzing sand grains is that it allows us to remove the sample from the beam and acquire μ -XRF images on the

Table 6 Linear combination fitting results showing combinations of two standards [goethite and Fe(III)-treated peat 3600 $^{\rm a}$] fit to individual Fe μ -XANES point spectra collected from individual sand grains from four soil samples (fits are overlaid on spectra in Fig. 6).

Sample ID	Fe fluorescence intensity (log values)	As fluorescence intensity (log values)	Proportions of standards ± uncertainty		R- factor
			goethite	Fe(III)- peat 3600 ^a	
Buncombe B #1					
1	9.8	7.4	15 ± 8	85 ± 8	0.0013
2	10.1	5.4	0	$100~\pm$	0.0012
3	10.5	7.1	34 ± 8	66 ± 7	0.0012
4	10.6	7.4	53 ± 5	47 ± 5	0.0014
5	9.9	5.4	7 ± 8	93 ± 8	0.0015
6	10.4	8.0	14 ± 10	$\begin{array}{c} 86 \; \pm \\ 10 \end{array}$	0.0022
7	10.8	7.4	94 ± 9	6 ± 8	0.0017
8	11.2	8.5	22 ± 10	$\begin{array}{c} 78 \; \pm \\ 10 \end{array}$	0.0022
9	10.8	8.5	0	$\begin{array}{c} 100 \ \pm \\ 7 \end{array}$	0.0025
10	10	7.4	0	100 ± 9	0.0038
11	10.2	7.3	0	$100\ \pm$ 16	0.0057
12	10.2	6.9	100 ± 0	0	0.0006
13	10	6.9	13 ± 4	87 ± 4	0.001
14	10.8	8.3	43 ± 5	57 ± 5	0.0013
Fripp A #1					
1	9.5	5.0	0	100 ± 9	0.0017
2	9.3	5.4	0	100 ± 7	0.0011
3	9.2	5.8	0	$\begin{array}{c} 100\ \pm \\ 7 \end{array}$	0.001
Fripp B #1					
1	11.6	8.4	53 ± 6	47 ± 6	0.0007
2	11.4	8.4	38 ± 5	62 ± 5	0.0007
3	11	7.9	0	$\begin{array}{c} 100\ \pm \\ 5 \end{array}$	0.0014
4	9.8	7.3	0	$\begin{array}{c} 100\ \pm \\ 7 \end{array}$	0.001
5	9.8	7.4	0	100 ±	0.0013
6	10.2	7.6	0	100 ± 9	0.0017
Osier Bw #2					
1	10	7.3	0	100 ± 7	0.0011
2	11.2	6.8	26 ± 5	774 ± 5	0.0011
3	10.8	5.8	0	100 ±	0.0011
				6	
4	8.7	7.3	0	100 ± 5	0.0027

^a Fe(III) treated peat samples with Fe reacted at 3600 mmol Fe/kg peat.

same area before and after As(V) treatment to assess short-term reactivity of As(V). Natural sand grains are not perfectly flat or smooth, hence areas on the surface where good signals could be obtained and signal attenuation could be avoided (for e.g., relatively flat regions rather than the crevices) were selected for analyses. Although natural samples are often thin sectioned to achieve flat samples (Gillispie et al., 2016; Gillispie et al., 2019; Langner et al., 2013; Strawn et al., 2002), thin sectioning of the sand grains precludes us from treating the grain coatings with As(V), and therefore natural sand grains were used for analyses.

For the objective of our work, which is to determine if there is

variation in As accumulation in soil microsites that are isolated from soils with contrasting properties, different microsites from different grains were selected. The selected microsites contained suites of elements and represented the natural soil setting. Also, the images of selected microsites contained large numbers of data points (i.e., 10,000), which is sufficient for statistical analyses (Guinness et al., 2014; Terres et al., 2018).

4.2. Contributions of multiple-elements to As accumulation in soil microsites

Overall, our statistical modeling of μ -XRF images and μ -XANES spectral analyses inferred that arsenate reactivity and binding depended on the combination of elements within microscale regions of soil matrices developed within or across different pedogenic environments. The non-spatial, predictive models from μ -XRF images and results of LCF analysis of As μ -XANES spectra suggested that Fe was consistently the most dominant matrix element predicting As retention within soil microsites, with varying degrees of augmentation by solids containing Mn, Ti, Zn or Cu (Tables 3, A.5). This evidence for preferential As(V) binding to Fe (hydr)oxides on the coatings of sand grains evaluated here is consistent with high-affinity bonding of arsenate to various Fe (hydr) oxides as inner-sphere surface complexes, which have been deduced from studies on model systems (Di Iorio et al., 2018; Dzade and De Leeuw, 2018; Fendorf et al., 1997; Manceau, 1995; Waychunas et al., 1995).

The inclusion of Mn, Ti, Cu or Zn in our statistical models for describing As accumulation suggests that Fe-(hydr)oxides alone do not account for As binding; however, the mechanisms of enhanced As retention by solids containing these elements are not clear. Studies have shown that under natural conditions, Mn oxides co-localized with Fe can enhance As(V) accumulation by preventing reductive dissolution of Fe oxides; Mn oxides act as a redox buffer (Borch et al., 2010; Gillispie et al., 2019). Additionally, Mn oxides can rapidly oxidize As(III) to As (V), enhancing adsorption of As(V) to Fe (hydr)oxides and Mn oxides (Lafferty et al., 2010; Manning et al., 2002; Wu et al., 2018; Ying et al., 2012). Arsenic(V) most likely coordinates with MnO₂ via bidentate binuclear corner sharing complex (Lafferty et al., 2010; Manning et al., 2002). We reacted our samples with As(V), and As μ -XANES spectral fits only showed evidence for minor (<10%) As(III) in one sample (Osier Bw #2-H). This sample was derived from a soil developed under the most reducing pedogenic conditions, as implied from characteristics in Table 1 and soil classification. Iron μ-XANES spectra showed no evidence for reduced Fe in any of our samples, and area-averaged µ-XRF signals indicated that Mn was less abundant than Fe in all samples (Table A.3).

Enhanced As(V) sorption by Fe (hydr)oxides in the presence of Zn, Cu, or Ti has been shown from studies on model systems (Gräfe et al., 2004; Rao et al., 2015; Zhang et al., 2013). Similarly, As adsorption was enhanced when Fe, Ti and Mn co-existed as a composite oxide (Zhang et al., 2018b). However, such effects cannot be isolated at the microscale of μ -XRF imaging. Also, although we could not detect Al by μ -XRF analysis, significant contributions of Al (hydr)oxides to As retention in our soil samples was implied by: (i) a greater abundance of Al and a weak but significant correlation (r'>0.11) between Al and Fe determined by TOF-SIMS analysis (Fig. 3); (ii) As μ -XANES fits that included 13–28% of a standard of arsenate adsorbed on boehmite (Table 4); and (iii) a documented adsorption capacity of Al (hydr)oxides for arsenate reported for model systems (Goldberg, 2002; Violante and Pigna, 2002).

Collectively, the statistical relationships between accumulated As and soil matrix elements were found to be highly variable within and between soils. Differences in partial correlation and regression coefficients found in two regions of the same sand grain, as well as between the two sand grains from the same soil (Tables 2 and 3) indicate that the degree of heterogeneity of matrix element affects As accumulation irrespective of pedogenic environment. In essence, our results indicate

A. Sharma et al. Geoderma 411 (2022) 115697

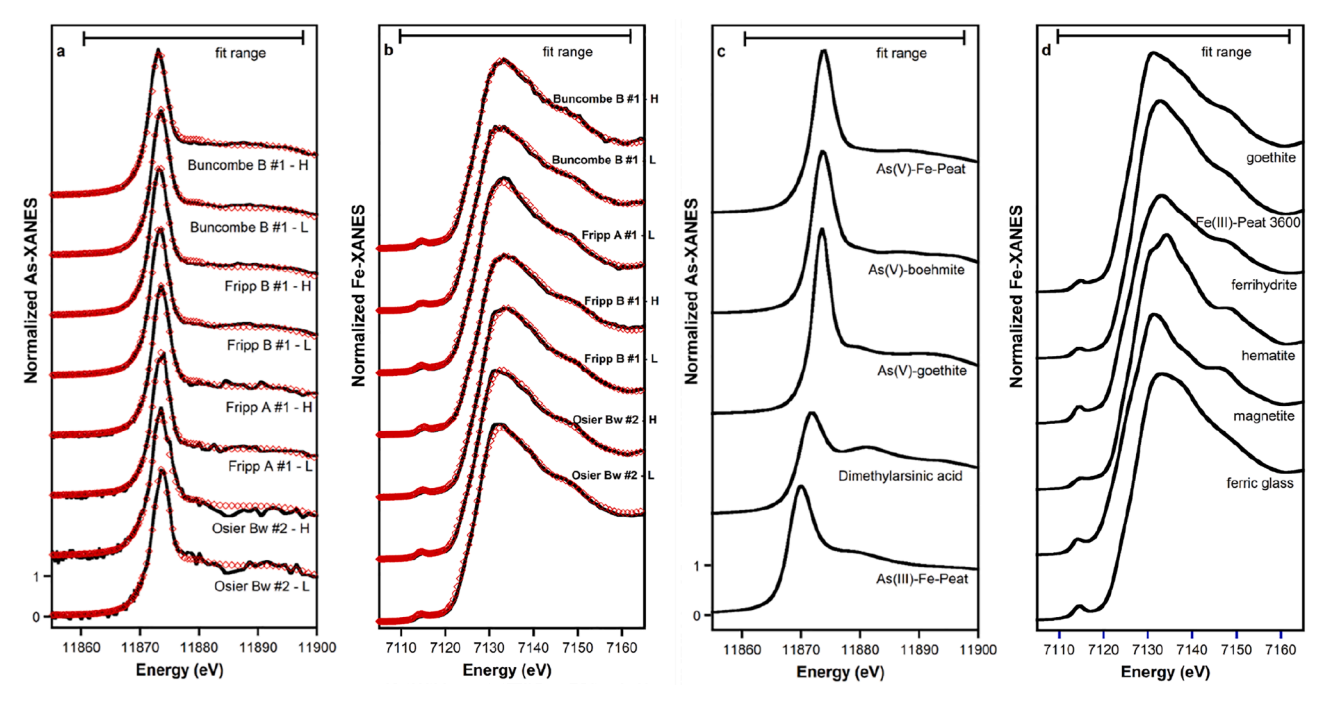


Fig. 5. Arsenic and iron K-edge XANES spectra: merged As μ -XANES spectra (black lines) with overlaid fits (red points) corresponding with models tabulated in Table 4 for high (H) and low (L) Fe regions (a); merged Fe μ -XANES spectra and overlaid fits (Table 5) for high and low As regions (b); and bulk spectra for As (c) and Fe (d) standards included in linear-combination fitting analyses. Regions that have >50% or \leq 50% of the maximum fluorescence signal of As/Fe are determined as high (H) or low (L) As/Fe regions. (For interpretation of the references to colour in this figure legend, the reader is referred to the web version of this article.)

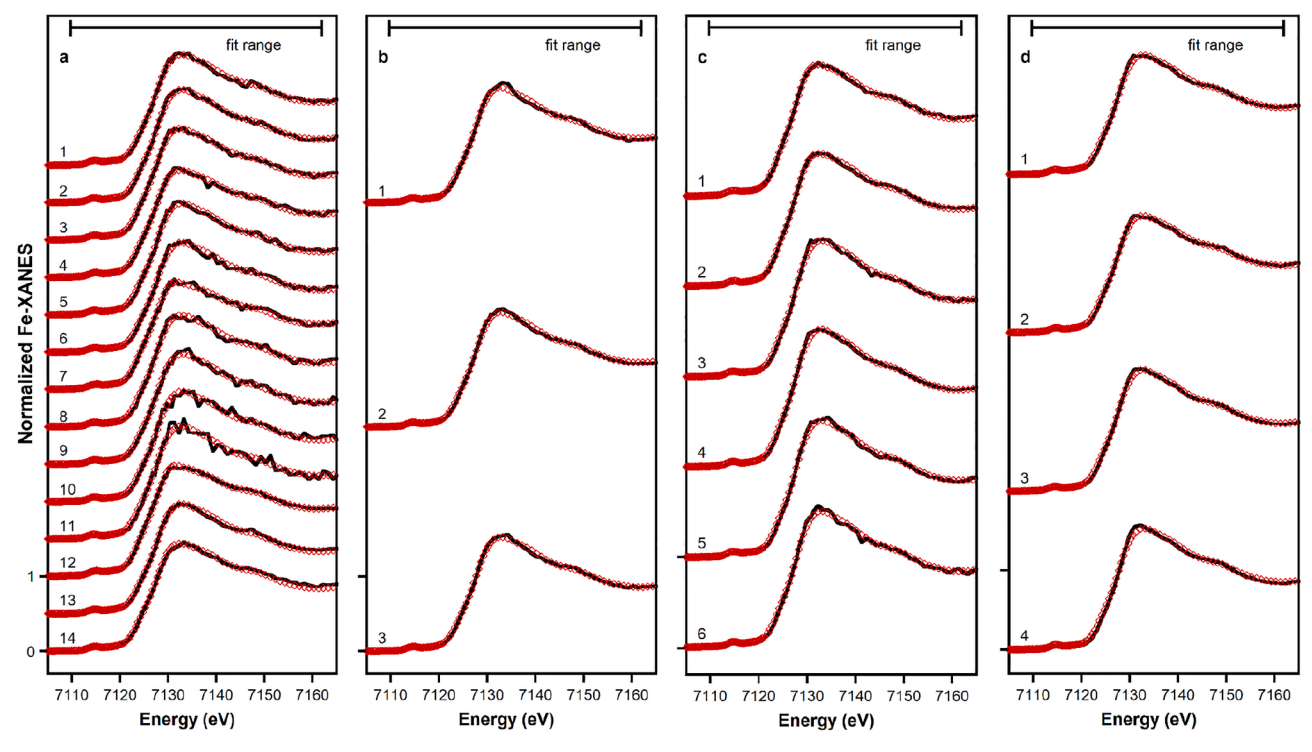


Fig. 6. Individual Fe K-edge μ-XANES spectra (black lines) collected from Buncombe B #1 (a), Fripp A #1 (b), Fripp B #1 (c), and Osier Bw #2 (d), along with overlaid fits (red points) corresponding with models tabulated in Table 6. Numbers on each μ-XANES spectrum correspond to spots denoted in Fig. 2. Spectra that fall under high As region include: 6, 8, 9, 10, and 14 for Buncombe B #1; 1, 2, 3, 5, and 6 for Fripp B #1, and 1, 2, and 4 for Osier Bw #2. All three spectra for Fripp A #1 fall under the low As region. (For interpretation of the references to colour in this figure legend, the reader is referred to the web version of this article.)

that microscale variations in matrix composition affect As accumulation, and Fe, Al, as well as less abundant Mn, Zn, Ti, and Cu contribute to the differences in As accumulation. In light of the studies that showed effects of microscale heterogeneity on As accumulation (Gillispie et al., 2019; Strawn et al., 2002), it is important to consider chemical heterogeneity within microenvironments to more accurately predict As mobility.

4.3. Influence of Fe on As accumulation in diverse microsites

Numerous studies have shown high-affinity, inner-sphere surface complexation of As(V) by Fe in Fe(III) (hydr)oxides as discussed above. However, the amount of accumulated As on the solids depends on the redox state of the soil, where the Fe and As content in the solids are controlled likely due to reductive dissolution of Fe(III) oxides (Bennett and Dudas, 2003; Erbs et al., 2010; Schaefer et al., 2017; Schwertmann, 1991). Therefore, one can expect to have variations in Fe contributions to accumulation of As in different soils.

Our regression models from $\mu\text{-XRF}$ images indicated that the contribution of Fe to accumulate As varied across soil microsites, indicated by differences in regression coefficients for Fe which ranged from 0.14 to 1.01 (Table 3 and A.5). Such variations in Fe contributions is conceivable because the soils which developed under poorer drainage conditions, such as the Osier soil sampled here, are exposed to more reducing conditions. Such conditions are expected to have different proportions of crystalline vs. poorly crystalline forms of Fe (hydr)oxides because of more frequent reductive dissolution-oxidative precipitation cycles (Schwertmann, 1993). Poorly crystalline Fe (hydr)oxides adsorb four- to five-fold more arsenate than goethite, at a given pH (Violante and Pigna, 2002). Our Osier Bw sample showed the least amount of total Fe content (Table 1) in the bulk sample and a dominant fit with the Fe (III)-treated peat standard (Table 6), a poorly crystalline form of Fe. It is noteworthy, however, that As accumulation in ROI-100a of our Osier Bw #2 grain was minimally greater than the native As detected by μ -XRF analysis in this sample region. Sand grains from well-drained soils, particularly the Buncombe B sample, showed the greatest amount of total Fe in the bulk sample (Table 1) and Fe μ-XANES fits for this soil showed a greater average proportion of a goethite standard (28 \pm 34%, n = 14) compared with the samples of Fripp A (none detected in three spots), Fripp B (15 \pm 24%; n = 6), or Osier Bw (6 \pm 13%) samples, although the results are highly variable (Table 6). Another interesting result was found in sample Fripp B #1-ROI-100a, where the accumulated As appeared to be nearly as high as for Buncombe B#1-ROI-100a despite having a relatively low Fe content. This could be attributed to the contribution of Al on As accumulation, which is supported by As μ-XANES fits that indicated the As(V) bound to Al standard accounting for 13% of the spectral features in this sample (Table 4), and the bulksoil analysis showed a considerable amount of Al (2000 mg/kg -Table A.2) present in this soil. Finally, we also wanted to point out that while the LCF results of Fe μ-XANES suggested the predominance of Fe (III) bound to peat standard, the fit results of As μ-XANES suggested the predominance of As(V) bound to goethite. This result suggests a higher affinity of As(V) for goethite in the sample. Although intrinsic surface complexation constants for As(V) are higher for goethite than amorphous iron oxide (Dixit and Hering, 2003), interpretation of spectral fits from our heterogeneous samples in terms of definitive speciation is only tentative (Sharma and Hesterberg, 2020).

While statistical analyses of μ -XRF images and μ -XANES spectral analyses allowed us to decouple the effects of co-localized elements on As accumulation, the ability of the micro-focused techniques to decouple the effects of co-localized matrix elements more accurately is limited by the micron-scale spatial resolution of the microprobe. Soil heterogeneity persists even at the smallest spatial scale (e.g., sub-micrometer) and probing a soil matrix with a probesize larger than the size of the solid phase provides only average information. A high resolution probe (for e. g., nanoprobe) would be more ideal to capture submicroscale soil heterogeneity and unmask the effects of co-localized elements on As

accumulation.

5. Conclusions

Multivariate statistical models and partial correlation analyses of $\mu\textsc{-}XRF$ images combined with $\mu\textsc{-}XANES$ spectroscopic analyses of As(V)-treated sand grains showed significant variations in geochemical effects of matrix elements on As retention. Such variations were evident between imaged areas of sand grains from within one soil as well as between different areas of a single sand grain. In fact, variations in the relative importance of each predictor element between different microsites were found. These results indicated that the degree of microscale heterogeneity of matrix elements affects As accumulation regardless of the pedogenic environment.

Our collective results implied that both Fe and Al (hydr)oxides were dominant soil components responsible for As(V) retention in these soil matrices and microsites, consistent with the high-affinity adsorption of arsenate shown for these adsorbents in model systems. However, our statistical analyses also inferred that As binding was enhanced by less abundant Mn, Zn, Ti, and Cu in solids within microsites of our samples. We cannot determine at the spatial scale of our μ-XRF data whether Ti, Zn, or Cu bearing solids were present in distinctly separated phases within microsites versus associated into complex, submicrometer-sized assemblages. However, given that co-localization of Fe and Ti is evident, it is possible that Ti is structurally incorporated in iron oxides. Titanium is commonly found to be combined with Fe in soils, and direct replacement of Fe by Ti within goethite has been reported (Fitzpatrick et al., 1978; Wells et al., 2006). Similarly, Zn and Cu are also reported to associate with goethite, with some proportions of these elements being present in the structure of the iron oxides (Manceau et al., 2000; Singh and Gilkes, 1992). Elucidating possible mechanisms by which Ti, Cu or Zn enhance As accumulation would require analyses that are more targeted to these elements, for e.g., μ -XAS analyses at the Ti, Cu, and Zn edges.

More than 95% of trace elements are sequestered in soil solids via formation of strong surface complexes; however, minor changes in aqueous concentrations can have a disproportionate effect on element toxicity (Hesterberg, 1998; McBride, 1989). Thus, even a minor contribution of matrix elements to enhance As immobilization could play an important role in minimizing environmental impacts of As release. Our results suggested that minor matrix elements such as Mn, Ti, Zn, or Cu are potentially important in terms of their contribution to As immobilization. Therefore, the impacts of these minor soil-matrix elements on immobilizing As and the underlying molecular mechanisms of immobilization are important next steps for future research, specifically, the multicomponent heterogeneities affecting trace element binding in geochemical matrices.

Funding

This material is based upon work supported by the National Science Foundation (NSF) under Grant No. EAR-1349374. This research used the SRX (5-ID) beamline of the National Synchrotron Light Source II, a U.S. Department of Energy (DOE) Office of Science User Facility operated for the DOE Office of Science by Brookhaven National Laboratory under Contract No. DE-SC0012704. This work was performed in part at the Analytical Instrumentation Facility (AIF) at NC State University, which is supported by the State of North Carolina and the NSF (award# ECCS-1542015). The AIF is a member of the North Carolina Research Triangle Nanotechnology Network (RTNN), a site in the National Nanotechnology Coordinated Infrastructure (NNCI).

Declaration of Competing Interest

The authors declare that they have no known competing financial interests or personal relationships that could have appeared to influence

A. Sharma et al. Geoderma 411 (2022) 115697

the work reported in this paper.

Acknowledgments

The authors are grateful to Dr. Juergen Thieme and Dr. Garth Williams (Brookhaven National Laboratory) for their assistance in data collection at the SRX beamline and to Dr. Chuanzhen Elaine Zhou for her assistance in collecting TOF-SIMS data. We are also thankful to Kim Hutchison for laboratory support, to Jonathan Sawyer and Sarah Dance for their support during the experiment at SRX, to Joshua Sanchez and Dr. Donald Sparks (University of Delaware) for providing As(V)-goethite standard, and to Dr. Matthew Siebecker (Texas Tech University) for providing great feedback on the manuscript.

Appendix A. Supplementary data

Supplementary data to this article can be found online at https://doi. org/10.1016/j.geoderma.2022.115697.

References

- Amstaetter, K., Borch, T., Larese-Casanova, P., Kappler, A., 2010. Redox transformation of arsenic by Fe (II)-activated goethite (α-FeOOH). Environ. Sci. Technol. 44 (1),
- Arai, Y., Livi, K.J., 2013. Underassessed phosphorus fixation mechanisms in soil sand fraction. Geoderma 192, 422-429.
- Beale, C.M., Lennon, J.J., Yearsley, J.M., Brewer, M.J., Elston, D.A., 2010. Regression analysis of spatial data. Ecol. Lett. 13 (2), 246-264.
- Bennett, B., Dudas, M.J., 2003. Release of arsenic and molybdenum by reductive dissolution of iron oxides in a soil with enriched levels of native arsenic. J. Environ. Eng. Sci. 2 (4), 265-272.
- Bhowmick, S., Pramanik, S., Singh, P., Mondal, P., Chatterjee, D., Nriagu, J., 2018 Arsenic in groundwater of West Bengal, India: A review of human health risks and assessment of possible intervention options. Sci. Total Environ. 612, 148-169.
- Borch, T., Kretzschmar, R., Kappler, A., Cappellen, P.V., Ginder-Vogel, M., Voegelin, A., Campbell, K., 2010. Biogeochemical redox processes and their impact on contaminant dynamics. Environ. Sci. Technol. 44 (1), 15-23.
- Brammer, H., Ravenscroft, P., 2009. Arsenic in groundwater: a threat to sustainable agriculture in South and South-east Asia. Environ. Int. 35 (3), 647-654.
- Buol, S., Southard, R., Graham, R., McDaniel, P., 2003. Soil genesis and classification, 5th edn. Iowa State University Press, Ames, IA.
- Burton, E.D., Johnston, S.G., Kocar, B.D., 2014. Arsenic mobility during flooding of contaminated soil; the effect of microbial sulfate reduction, Environ, Sci. Technol, 48 (23), 13660-13667.
- Burton, E.D., Karimian, N., Johnston, S.G., Schoepfer, V.A., Choppala, G., Lamb, D., 2021. Arsenic-Imposed Effects on Schwertmannite and Jarosite Formation in Acid Mine Drainage and Coupled Impacts on Arsenic Mobility. ACS Earth Space Chem. 5
- Chen, C., Sparks, D.L., 2015. Multi-elemental scanning transmission X-ray microscopy-near edge X-ray absorption fine structure spectroscopy assessment of organo-mineral associations in soils from reduced environments. Environ. Chem. 12
- Chen, C., Sparks, D.L., 2018. Fe (II)-Induced Mineral Transformation of Ferrihydrite-Organic Matter Adsorption and Co-precipitation Complexes in the Absence and Presence of As (III). ACS Earth Space Chem. 2 (11), 1095-1101.
- Cheng, H., Hu, Y., Luo, J., Xu, B., Zhao, J., 2009. Geochemical processes controlling fate and transport of arsenic in acid mine drainage (AMD) and natural systems. J. Hazard. Mater. 165 (1-3), 13-26.
- Chen-Wiegart, Y.-c.K., Williams, G., Zhao, C., Jiang, H., Li, L., Demkowicz, M., Seita, M., Short, M., Ferry, S., Wada, T., 2016. Early science commissioning results of the submicron resolution X-ray spectroscopy beamline (SRX) in the field of materials science and engineering, AIP Conference Proceedings. AIP Publishing, pp. 030004.
- Di Iorio, E., Cho, H.G., Liu, Y., Cheng, Z., Angelico, R., Colombo, C., 2018. Arsenate retention mechanisms on hematite with different morphologies evaluated using AFM, TEM measurements and vibrational spectroscopy. Geochim. Cosmochim. Acta 237, 155-170.
- Dixit, S., Hering, J.G., 2003. Comparison of arsenic (V) and arsenic (III) sorption onto iron oxide minerals: implications for arsenic mobility. Environ. Sci. Technol. 37 (18), 4182-4189.
- Dzade, N.Y., de Leeuw, N.H., 2018. Density functional theory characterization of the structures of H3AsO3 and H3AsO4 adsorption complexes on ferrihydrite. Environ. Sci.: Processes Impacts 20 (6), 977-987.
- EPA, D., 1996. Method 3050B. Acid digestion of sediments, sludges, and soils. Revision 2. Test Methods for Evaluating Solid Wastes: Physical/Chemical Methods, EPA SW-846Section a, 3050B-3051e3050B.
- Erbs, J.J., Berquó, T.S., Reinsch, B.C., Lowry, G.V., Banerjee, S.K., Penn, R.L., 2010. Reductive dissolution of arsenic-bearing ferrihydrite. Geochim. Cosmochim. Acta 74 (12), 3382-3395.
- Fan, J.-X., Wang, Y.-J., Liu, C., Wang, L.-H., Yang, K.e., Zhou, D.-M., Li, W., Sparks, D.L., 2014. Effect of iron oxide reductive dissolution on the transformation and

- immobilization of arsenic in soils: New insights from X-ray photoelectron and X-ray absorption spectroscopy. J. Hazard. Mater. 279, 212-219.
- Fendorf, S., Kocar, B.D., 2009. Biogeochemical processes controlling the fate and transport of arsenic: implications for South and Southeast Asia. Adv. Agronomy 104,
- Fendorf, S., Eick, M.J., Grossl, P., Sparks, D.L., 1997. Arsenate and chromate retention mechanisms on goethite. 1. Surface structure. Environ. Sci. Technol. 31 (2),
- Fendorf, S., Nico, P.S., Kocar, B.D., Masue, Y., Tufano, K.J., 2010. Arsenic chemistry in soils and sediments. In: Developments in Soil Science. Elsevier, pp. 357-378.
- Fitzpatrick, R., Le Roux, J., Schwertmann, U., 1978. Amorphous and crystalline titanium and iron-titanium oxides in synthetic preparations, at near ambient conditions, and in soil clays. Clays Clay Miner. 26 (3), 189-201.
- Galkaduwa, M.B., Hettiarachchi, G.M., Kluitenberg, G.J., Hutchinson, S.L., 2018. Iron oxides minimize arsenic mobility in soil material saturated with saline wastewater. J. Environ. Qual. 47 (4), 873-883.
- Gamble, A.V., Givens, A.K., Sparks, D.L., 2018. Arsenic speciation and availability in orchard soils historically contaminated with lead arsenate. J. Environ. Qual. 47 (1),
- Gee, G.W., Bauder, J.W., 1986. Particle-size analysis. Methods of soil analysis: Part 1 Physical and mineralogical methods 5, 383-411.
- Gillispie, E.C., Andujar, E., Polizzotto, M.L., 2016. Chemical controls on abiotic and biotic release of geogenic arsenic from Pleistocene aquifer sediments to groundwater. Environ. Sci.: Processes Impacts 18 (8), 1090–1103.
- Gillispie, E.C., Matteson, A.R., Duckworth, O.W., Neumann, R.B., Phen, N., Polizzotto, M. L., 2019. Chemical variability of sediment and groundwater in a Pleistocene aquifer of Cambodia: implications for arsenic pollution potential. Geochim. Cosmochim. Acta 245, 441-458.
- Goldberg, S., 2002. Competitive adsorption of arsenate and arsenite on oxides and clay minerals. Soil Sci. Soc. Am. J. 66 (2), 413–421.
- Gräfe, M., Nachtegaal, M., Sparks, D.L., 2004. Formation of metal- arsenate precipitates at the goethite- water interface. Environ. Sci. Technol. 38 (24), 6561-6570.
- Gräfe, M., Tappero, R.V., Marcus, M.A., Sparks, D.L., 2008. Arsenic speciation in multiple metal environments: II. Micro-spectroscopic investigation of a CCA contaminated soil. J. Colloid Interface Sci. 321 (1), 1-20.
- Guinness, J., 2018b. Permutation and grouping methods for sharpening Gaussian process approximations. Technometrics 60 (4), 415–429.
- Guinness, J., Fuentes, M., Hesterberg, D., Polizzotto, M., 2014. Multivariate spatial modeling of conditional dependence in microscale soil elemental composition data. Spatial Stat. 9, 93-108.
- Guinness, J., 2018a. Fast Gaussian Process Computation Using Vecchia's Approximation. Web. https://cran.r-project.org/web/packages/GpGpGpDpdf>.
 Hesterberg, D., 1998. Biogeochemical cycles and processes leading to changes in
- mobility of chemicals in soils. Agric., Ecosyst. Environ. 67 (2-3), 121-133.
- Hesterberg, D., Duff, M.C., Dixon, J.B., Vepraskas, M.J., 2011. X-ray microspectroscopy and chemical reactions in soil microsites. J. Environ. Qual. 40 (3), 667-678.
- Inskeep, W.P., McDermott, T.R., Fendorf, S., 2001. Arsenic (V)/(lll) cycling in soils and natural waters: chemical and microbiological processes. Environ. Chem. Arsenic 183-215.
- Jackson, M.L., Lim, C.H., Zelazny, L.W., 1986. Oxides, hydroxides, and aluminosilicates. Methods of Soil Analysis: Part 1 Physical and Mineralogical. Methods 5, 101–150.
- Johnston, S.G., Keene, A.F., Burton, E.D., Bush, R.T., Sullivan, L.A., McElnea, A.E., Ahern, C.R., Smith, C.D., Powell, B., Hocking, R.K., 2010. Arsenic mobilization in a seawater inundated acid sulfate soil. Environ. Sci. Technol. 44 (6), 1968–1973.
- Karimian, N., Johnston, S.G., Burton, E.D., 2017. Effect of cyclic redox oscillations on water quality in freshwater acid sulfate soil wetlands. Sci. Total Environ. 581-582, 314-327
- Kelly, S., Hesterberg, D., Ravel, B., 2008. Analysis of soils and minerals using X-ray absorption spectroscopy. Methods of soil analysis. Part 5 387-464.
- Kizewski, F., Liu, Y.-T., Morris, A., Hesterberg, D., 2011. Spectroscopic approaches for phosphorus speciation in soils and other environmental systems. J. Environ. Qual. 40 (3), 751-766.
- Kocar, B.D., Fendorf, S., 2012, Arsenic release and transport in sediments of the Mekong Delta. Interdisc. Stud. Environ. Chem.-Environ. Pollut. Ecotoxicol. 117-124.
- Lafferty, B.J., Ginder-Vogel, M., Zhu, M., Livi, K.J.T., Sparks, D.L., 2010. Arsenite oxidation by a poorly crystalline manganese-oxide. 2. Results from X-ray absorption spectroscopy and X-ray diffraction. Environ. Sci. Technol. 44 (22), 8467-8472.
- Landrot, G., Tappero, R., Webb, S.M., Sparks, D.L., 2012. Arsenic and chromium speciation in an urban contaminated soil. Chemosphere 88 (10), 1196-1201.
- Langner, P., Mikutta, C., Suess, E., Marcus, M.A., Kretzschmar, R., 2013. Spatial distribution and speciation of arsenic in peat studied with microfocused X-ray fluorescence spectrometry and X-ray absorption spectroscopy. Environ. Sci. Technol. 47 (17), 9706-9714.
- LeMonte, J.J., Stuckey, J.W., Sanchez, J.Z., Tappero, R., Rinklebe, J., Sparks, D.L., 2017. Sea level rise induced arsenic release from historically contaminated coastal soils. Environ. Sci. Technol. 51 (11), 5913-5922.
- Li, L., Yan, H., Xu, W., Yu, D., Heroux, A., Lee, W.-K., Campbell, S.I., Chu, Y.S., 2017. PyXRF: Python-based X-ray fluorescence analysis package, X-Ray Nanoimaging: Instruments and Methods III. International Society for Optics and Photonics, pp. 103890U.
- Li, R., Kuo, Y.-M., Liu, W.-W., Jang, C.-S., Zhao, E., Yao, L., 2018. Potential health risk assessment through ingestion and dermal contact arsenic-contaminated groundwater in Jianghan Plain, China. Environ. Geochem. Health 40 (4), 1585-1599.
- Lopez, A.R., Silva, S.C., Webb, S.M., Hesterberg, D., Buchwalter, D.B., 2018. Periphyton and abiotic factors influencing arsenic speciation in aquatic environments. Environ. Toxicol. Chem. 37 (3), 903-913.

A. Sharma et al. Geoderma 411 (2022) 115697

- Ma, M., Dalling, J.W., Ma, Z., Zhou, X., 2017. Soil environmental factors drive seed density across vegetation types on the Tibetan Plateau. Plant Soil 419 (1-2), 349, 361
- Manceau, A., 1995. The mechanism of anion adsorption on iron oxides: evidence for the bonding of arsenate tetrahedra on free Fe (O, OH) 6 edges. Geochim. Cosmochim. Acta 59 (17), 3647–3653.
- Manceau, A., Schlegel, M.L., Musso, M., Sole, V.A., Gauthier, C., Petit, P.E., Trolard, F., 2000. Crystal chemistry of trace elements in natural and synthetic goethite. Geochim. Cosmochim. Acta 64 (21), 3643–3661.
- Manceau, A., Tamura, N., Marcus, M.A., MacDowell, A.A., Celestre, R.S., Sublett, R.E., Sposito, G., Padmore, H.A., 2002. Deciphering Ni sequestration in soil ferromanganese nodules by combining X-ray fluorescence, absorption, and diffraction at micrometer scales of resolution. Am. Mineral. 87 (10), 1494–1499.
- Manceau, A., Lanson, M., Takahashi, Y., 2014. Mineralogy and crystal chemistry of Mn, Fe Co, Ni, and Cu in a deep-sea Pacific polymetallic nodule. Am. Mineral. 99 (10), 2068–2083.
- Manning, B.A., Fendorf, S.E., Bostick, B., Suarez, D.L., 2002. Arsenic (III) oxidation and arsenic (V) adsorption reactions on synthetic birnessite. Environ. Sci. Technol. 36 (5) 976–981
- McBride, M., 1989. Reactions controlling heavy metal solubility in soils. In: Advances in Soil Science. Springer, New York, NY, pp. 1–56.
- Mikutta, C., Kretzschmar, R., 2011. Spectroscopic evidence for ternary complex formation between arsenate and ferric iron complexes of humic substances. Environ. Sci. Technol. 45 (22), 9550–9557.
- Minasny, B., McBratney, A.B., 2005. The Matérn function as a general model for soil variograms. Geoderma 128 (3-4), 192–207.
- Minasny, B., McBratney, A.B., 2007. Spatial prediction of soil properties using EBLUP with the Matérn covariance function. Geoderma 140 (4), 324–336.
- Muedi, K.L., Brink, H.G., Masindi, V., Maree, J.P., 2021. Effective removal of arsenate from wastewater using aluminium enriched ferric oxide-hydroxide recovered from authentic acid mine drainage. J. Hazard. Mater. 414, 125491.
- NCSU-AIF, 2018. TOF-SIMS-general-experiment-description. https://www.aif.ncsu.edu/wp-content/uploads/sites/25/2013/05/TOF-SIMS-general-experiment-description.
- pdf.
 Otero-Fariña, A., Fiol, S., Arce, F., Antelo, J., 2017. Effects of natural organic matter on
- the binding of arsenate and copper onto goethite. Chem. Geol. 459, 119–128. Paikaray, S., 2015. Arsenic geochemistry of acid mine drainage. Mine Water Environ. 34 (2), 181–196.
- Park, J.H., Han, Y.-S., Ahn, J.S., 2016. Comparison of arsenic co-precipitation and adsorption by iron minerals and the mechanism of arsenic natural attenuation in a mine stream. Water Res. 106, 295–303.
- Polizzotto, M.L., Kocar, B.D., Benner, S.G., Sampson, M., Fendorf, S., 2008. Near-surface wetland sediments as a source of arsenic release to ground water in Asia. Nature 454 (7203), 505–508.
- Power, L.E., Arai, Y., Sparks, D.L., 2005. Zinc adsorption effects on arsenite oxidation kinetics at the birnessite— water interface. Environ. Sci. Technol. 39 (1), 181–187.
- Rao, P., Sun, Z., Zhang, W., Yao, W., Wang, L., Ding, G., 2015. Preparation and application of amorphous Fe–Ti bimetal oxides for arsenic removal. RSC Adv. 5 (109), 89545–89551.
- Ravel, B., Newville, M., 2005. ATHENA, ARTEMIS, HEPHAESTUS: data analysis for X-ray absorption spectroscopy using IFEFFIT. J. Synchrotron Radiat. 12 (4), 537–541.
- Raven, K.P., Jain, A., Loeppert, R.H., 1998. Arsenite and arsenate adsorption on ferrihydrite: kinetics, equilibrium, and adsorption envelopes. Environ. Sci. Technol. 32 (3), 344–349.
- Ravenscroft, P., Brammer, H., Richards, K., 2009. Arsenic Pollution: A Global Synthesis. John Wiley & Sons.
- Rehman, K., Fatima, F., Waheed, I., Akash, M.S.H., 2018. Prevalence of exposure of heavy metals and their impact on health consequences. J. Cell. Biochem. 119 (1), 157–184.
- Rivera, N., Kaur, N., Hesterberg, D., Ward, C.R., Austin, R.E., Duckworth, O.W., 2015. Chemical composition, speciation, and elemental associations in coal fly ash samples related to the Kingston ash spill. Energy Fuels 29 (2), 954–967.
- Schaefer, M.V., Guo, X., Gan, Y., Benner, S.G., Griffin, A.M., Gorski, C.A., Wang, Y., Fendorf, S., 2017. Redox controls on arsenic enrichment and release from aquifer sediments in central Yangtze River Basin. Geochim. Cosmochim. Acta 204, 104–119.
- Schwer, D.R., McNear, D.H., 2011. Chromated copper arsenate-treated fence posts in the agronomic landscape: soil properties controlling arsenic speciation and spatial distribution. J. Environ. Qual. 40 (4), 1172–1181.
- Schwertmann, U., 1991. Solubility and dissolution of iron oxides. Plant and soil 130 (1-2), 1-25
- Schwertmann, U., 1993. Relations between iron oxides, soil color, and soil formation. Soil color (soilcolor) 51–69.

Shakoor, M.B., Nawaz, R., Hussain, F., Raza, M., Ali, S., Rizwan, M., Oh, S.-E., Ahmad, S., 2017. Human health implications, risk assessment and remediation of Ascontaminated water: a critical review. Sci. Total Environ. 601-602, 756-769.

- Sharma, A., 2019. Arsenic Reactivity in Soil Microsites in Relation to Matrix Composition. NC State University, p. 237. Dissertation Thesis.
- Sharma, A., Hesterberg, D., 2020. Synchrotron radiation-based spatial methods in environmental biogeochemistry. Multidimensional Analytical Techniques in Environmental Research, eds. RMBO Duarte and AC Duarte (Elsevier, BV, 2020), 231-265
- Sharma, A., Muyskens, A., Guinness, J., Polizzotto, M.L., Fuentes, M., Tappero, R.V., Chen-Wiegart, Y.-C., Thieme, J., Williams, G.J., Acerbo, A.S., Hesterberg, D., 2019. Multi-element effects on arsenate accumulation in a geochemical matrix determined using µ-XRF, µ-XANES and spatial statistics. J. Synchrotron Radiat. 26 (6), 1967–1979.
- Singh, B., Gilkes, R., 1992. Properties and distribution of iron oxides and their association with minor elements in the soils of south-western Australia. J. Soil Sci. 43 (1), 77–98.
- Smedley, P.L., Kinniburgh, D.G., 2002. A review of the source, behaviour and distribution of arsenic in natural waters. Appl. Geochem. 17 (5), 517–568.
- Sparks, D.L., 1999. Kinetics and mechanisms of chemical reactions at the soil mineral/ water interface. Soil Phys. Chem. 2, 136–191.
- Strawn, D., Doner, H., Zavarin, M., McHugo, S., 2002. Microscale investigation into the geochemistry of arsenic, selenium, and iron in soil developed in pyritic shale materials. Geoderma 108 (3-4), 237–257.
- Sullivan, L.A., Bush, R.T., 2004. Iron precipitate accumulations associated with waterways in drained coastal acid sulfate landscapes of eastern Australia. Mar. Freshw. Res. 55 (7), 727–736.
- Tchounwou, P.B., Yedjou, C.G., Udensi, U.K., Pacurari, M., Stevens, J.J., Patlolla, A.K., Noubissi, F., Kumar, S., 2019. State of the science review of the health effects of inorganic arsenic: perspectives for future research. Environ. Toxicol. 34 (2), 188-202
- Terres, M.A., Fuentes, M., Hesterberg, D., Polizzotto, M., 2018. Bayesian spectral modeling for multivariate spatial distributions of elemental concentrations in soil. Bayesian Anal. 13 (1), 1–28.
- Thomas, G.W., 1996. Soil pH and soil acidity. Methods of soil analysis: part 3 chemical methods 5, 475-490.
- Tisdall, J.M., Oades, J.M., 1982. Organic matter and water-stable aggregates in soils. J. Soil Sci. 33 (2), 141–163.
- Violante, A., Pigna, M., 2002. Competitive sorption of arsenate and phosphate on different clay minerals and soils. Soil Sci. Soc. Am. J. 66 (6), 1788–1796.
- Waychunas, G.A., Davis, J.A., Fuller, C.C., 1995. Geometry of sorbed arsenate on ferrihydrite and crystalline FeOOH: re-evaluation of EXAFS results and topological factors in predicting sorbate geometry, and evidence for monodentate complexes. Geochim. Cosmochim. Acta 59 (17), 3655–3661.
- Wells, M.A., Fitzpatrick, R.W., Gilkes, R.J., 2006. Thermal and mineral properties of Al-Cr-, Mn-, Ni-and Ti-substituted goethite. Clays Clay Miner. 54 (2), 176–194.
- Wu, Y., Kukkadapu, R.K., Livi, K.J.T., Xu, W., Li, W., Sparks, D.L., 2018. Iron and arsenic speciation during As (III) oxidation by manganese oxides in the presence of Fe (II): molecular-level characterization using XAFS, Mössbauer, and TEM analysis. ACS Earth Space Chem. 2 (3), 256–268.
- Wuana, R.A., Okieimen, F.E., 2011. Heavy metals in contaminated soils: a review of sources, chemistry, risks and best available strategies for remediation. ISRN Ecol. 2011, 1–20.
- Yang, W., Kan, A.T., Chen, W., Tomson, M.B., 2010. pH-dependent effect of zinc on arsenic adsorption to magnetite nanoparticles. Water Res. 44 (19), 5693–5701.
- Ying, S.C., Kocar, B.D., Fendorf, S., 2012. Oxidation and competitive retention of arsenic between iron-and manganese oxides. Geochim. Cosmochim. Acta 96, 294–303.
- Ying, S.C., Masue-Slowey, Y., Kocar, B.D., Griffis, S.D., Webb, S., Marcus, M.A., Francis, C.A., Fendorf, S., 2013. Distributed microbially-and chemically-mediated redox processes controlling arsenic dynamics within Mn-/Fe-oxide constructed aggregates. Geochim. Cosmochim. Acta 104, 29–41.
- Zhang, W., Liu, C., Zheng, T., Ma, J., Zhang, G., Ren, G., Wang, L.u., Liu, Y., 2018a. Efficient oxidation and sorption of arsenite using a novel titanium (IV)-manganese (IV) binary oxide sorbent. J. Hazard. Mater. 353, 410–420.
- Zhang, G., Ren, Z., Zhang, X., Chen, J., 2013. Nanostructured iron (III)-copper (II) binary oxide: a novel adsorbent for enhanced arsenic removal from aqueous solutions. Water Res. 47 (12), 4022–4031.
- Zhang, W., Zhang, G., Liu, C., Li, J., Zheng, T., Ma, J., Wang, L.u., Jiang, J., Zhai, X., 2018b. Enhanced removal of arsenite and arsenate by a multifunctional Fe-Ti-Mn composite oxide: photooxidation, oxidation and adsorption. Water Res. 147, 264–275.